HELSINKI UNIVERSITY OF TECHNOLOGY
Faculty of Electronics, Communications and Automation

Jussi Mäkynen

A Lightweight Hyperspectral Imager

Master’s Thesis submitted in partial fulfilment of requirements for the degree of Master of Science in Technology

Espoo, November 11, 2009

Supervisor: Prof. Erkki Ikonen, Helsinki University of Technology
Instructor: Lic.Sc. (Tech.) Christer Holmlund, VTT Technical Research Centre of Finland

HELSINKI UNIVERSITY
OF TECHNOLOGY

ABSTRACT OF THE
MASTER'S THESIS

Author: Jussi Mäkynen

Title: A Lightweight Hyperspectral Imager

Date: November 11, 2009 **Number of pages:** 55+19

Department: Faculty of Electronics, Communications and Automation

Professorship: S-108 Measurement Science and Technology

Supervisor: Prof. Erkki Ikonen

Instructor: Lic.Sc. (Tech.) Christer Holmlund

In this work a control platform was designed for a hyperspectral imager. A hyperspectral imager is a spectrometer that can be used to obtain spectral data for each pixel in the image. The hyperspectral imager concept used in this work utilizes multiple transmission orders of a Fabry-Perot interferometer together with the different spectral sensitivities of RGB-image sensor pixels. With the built hyperspectral imager it is possible to acquire 2D spatial images at one, two or three selected wavelength bands simultaneously. By adjusting the transmission bands of the Fabry-Perot interferometer it is possible to measure the reflectance spectrum of the observed area.

The hyperspectral imager requires an accurate control mechanism for the interferometer mirrors as the air gap is controlled over a range of 600 nm to 3000 nm with one nanometre accuracy. The interferometer module used in this work is controlled with three piezoelectric actuators and the air gap is measured near each actuator to provide position information for the control system. A three channel closed-loop control system was designed and built for the interferometer module to control the parallelism and spacing between the mirror plates. A previous imaging system was modified to accommodate a flash memory which is used for saving the hyperspectral data.

The power consumption of the imager was measured to be 1.6 W and the total mass of the imager including the battery is 350 g. Several measurements were made to provide information on the system performance. The settling time for a 200 nm step change in the air gap was measured to be 0.6 ms. The noise induced air gap variation was estimated from the noise in the amplified error signal. The root-mean-square value of this movement was approximately 0.1 nm. The performance of the air gap control is decreased by the changes in the environment. The humidity of the environment changes the useful control range of the air gap. Temperature changed the air gap approximately 0.5 nm/°C.

Keywords: hyperspectral imager, Fabry-Perot interferometer, capacitive half bridge,
closed-loop control, flash memory

TEKNILLINEN KORKEAKOULU DIPLOMITYÖN TIIVISTELMÄ

Tekijä:	Jussi Mäkynen		
Työn nimi:	Kevytrakenteinen hyperspektrikamera		
Päivämäärä:	11.11.2009	**Sivuja:**	55+19
Osasto:	Elektroniikan, tietoliikenteen ja automaation tiedekunta		
Professuuri:	S-108 Mittaustekniikka		
Työn valvoja:	Prof. Erkki Ikonen		
Työn ohjaaja:	TkL Christer Holmlund		

Tässä työssä suunniteltiin ja toteutettiin ohjauselektroniikka hyperspektrikameraa varten. Hyperspektrikamera on spektrometri, jolla voidaan mitata spektri jokaiselle kuvan pikselille. Työssä käytetyn hyperspektraalisen kameran toiminta perustuu Fabry-Perot-interferometrin päästökaistojen ja värikuvasensorin pikseleiden toisistaan eroavien herkkyyksien hyödyntämiseen. Ohjaamalla interferometrin päästökaistoja sopivasti voidaan kuvasensorin eri pikseleiden avulla selvittää yhdestä kuvasta jopa kolmen spektrikaistan sisältö. Tutkittava spektrialue voidaan mitata muuttamalla transmissiokaistoja perättäisten kuvien välillä.

Toteutettu hyperspektraalinen kamera tarvitsee menetelmän, jolla interferometrin peilejä voidaan ohjata tarkasti. Interferometrin peilien välistä ilmarakoa tuli ohjata nanometrin tarkkuudella 600 nm - 3000 nm alueella. Työssä hyödynnettiin Fabry-Perot-interferometria, jonka ilmarakoa ohjataan kolmen pietsosähköisen aktuaattorin avulla. Interferometrin ilmarakoa mitataan kapasitiivisesti kolmesta kohdasta, mikä mahdollistaa takaisinkytketyn säädön toteuttamisen. Lisäksi aiemmin VTT:llä kehitettyyn kuvauselektroniikkaan lisättiin flash-muisti hyperspektraalisen tiedon tallentamiseksi.

Toteutetun hyperspektraalisen kameran tehon kulutus on vain 1.6 W. Kameran paino on noin 350 g. Työssä mitattiin myös interferometrin ja ohjauselektroniikan suorituskykyä. Interferometrin ilmaraon asettumisaika 200 nm askelmaiselle muutokselle on noin 0.6 ms. Kohinan aiheuttamaa ilmaraon muutosta arvioitiin mittaamalla kohina virhesignaalin esivahvistimen lähdössä ja laskemalla tätä kohinajännitettä vastaava ilmaraon muutos. Tämän arvioitiin olevan tehollisarvoltaan noin 0.1 nm. Ympäristön vaikutusten todettiin aiheuttavan suurimmat ongelmat ilmaraon ohjauksen tarkkuudessa. Varsinkin lämpötila ja kosteus vaikuttavat ohjauksen tarkkuuteen ja säätöalueeseen. Kosteus muuttaa lähinnä säätöaluetta, mutta lämpötila vaikuttaa myös ilmaraon asetusarvojen tarkkuuteen. Lämpötilan todettiin muuttavan ilmarakoa enimmillään 0.5 nm/°C.

Avainsanat: hyperspektraalinen kamera, Fabry-Perot-interferometri, kapasitiivinen mittaussilta, takaisinkytkentäinen säätö, flash-muisti

Preface

The work described in this Master’s thesis was conducted in the Optical Sensors team of VTT Technical Research Centre of Finland during 2009. The work was part of the Hanska project which was aiming at creating new business from optical hand held devices. I would like to thank all the project members for giving me this interesting and educational task.

I would like to thank my instructor Lic.Sc (Tech.) Christer Holmlund for his expert advice and guidance during this work. I would also like to thank my supervisor Prof. Erkki Ikonen for accepting to supervise this work.

I am grateful to all my fellow workers in the Optical sensors team for their help during this task and for creating a pleasant and inspiring working atmosphere. Special thanks go to my family and friends for their encouragements during my studies and especially during this work.

Espoo, November 09, 2009

Jussi Mäkynen

Table of Contents

Notations vii

Abbreviations ix

1 Introduction 1

2 Hyperspectral Imaging 2

3 The Fabry-Perot Interferometer 4

- 3.1 Theory 4
- 3.2 Interferometer Module 9

4 The Hyperspectral Imager Concept 11

- 4.1 Working Principle of the Hyperspectral Imager 11
- 4.2 Requirements for the Hyperspectral Imager Platform 14

5 Interferometer Control 16

- 5.1 Previous Control Systems 16
  - 5.1.1 Pressure Control 16
  - 5.1.2 Piezoelectric Actuators 16
  - 5.1.3 Optical Feedback 17
  - 5.1.4 Capacitive Feedback 17
- 5.2 Closed-Loop Control of the Interferometer 18
  - 5.2.1 Capacitive Half Bridge 19
  - 5.2.2 Control Loop 21

6 Electronics 22

- 6.1 Interferometer Module and Preamplifier Board 23
- 6.2 Gap Controller 24
  - 6.2.1 Square Wave Signals for the Capacitive Half Bridge 24

6.2.2 Control Loop....26
6.3 Image Sensor....29
6.4 Flash Memory....32
6.5 Spectrometer Control Board....34
6.5.1 Transferring Image Data to Flash Memory....35
6.5.2 Transferring Data to Computer....38

7 Control Software 40

7.1 User Program Functions....41

8 Measurements 42

8.1 Spectral Sampling Step Size....42
8.2 Preamplifier Noise....42
8.3 Air Gap Reproducibility....43
8.3.1 Temperature Characteristics....43
8.3.2 Drift Tests....45
8.4 Settling Time of the Interferometer Module....48
8.5 Average Power Consumption....49
8.6 Summary....49

9 The Hyperspectral Imager Tests 51

10 Conclusions 54

Bibliography 56

Appendix A 59

Hyperspectral Imager Parts....59

Appendix B 62

Preamplifier Noise and the Equivalent Change in the Air Gap....62

Notations

ε_air	Relative permittivity of air	
ε_0	Permittivity of vacuum	[F/m]
λ	Wavelength	[m]
ν_{FWHM}	Full-width at half-maximum in the frequency domain	[1/s]
φ_i	Spectral signal at the i^{th} transmission band	
ω	Angular frequency	[1/s]
A	Absorption	
A_r	Area of the capacitor electrodes	[m^2]
B_s	Signal of the blue pixel	[ADU]
c	Speed of light in vacuum	[m/s]
C_ref	Capacitance of the reference capacitor	[F]
C_m	Capacitance of the measurement electrodes	[F]
d	Distance between the capacitor electrodes	[m]
$\boldsymbol{E}$	Electric field strength	[V/m]
E_0	Electric field amplitude	[V/m]
F	Finesse	
F'	Coefficient of finesse	
FSR	Free spectral range	[1/s]

G_s	Signal of the green pixel	[ADU]
k	Angular wave number	[1/m]
L	Distance between interferometer mirrors	[m]
n	Refractive index	
r_{ij}	Reflection coefficient	
R	Reflectivity	
R_s	Signal of the red pixel	[ADU]
S_{nR}	Sensitivity of the red pixel for the signal in the n:th transmission band, where $n = 1, 2, 3\ldots$	
S_{nG}	Sensitivity of the green pixel for the signal in the n:th transmission band, where $n = 1, 2, 3\ldots$	
S_{nB}	Sensitivity of the blue pixel for the signal in the n:th transmission band, where $n = 1, 2, 3\ldots$	
t	Time	[s]
T	Transmission	
t_{ij}	Transmission coefficient	
V_{ref}	Reference voltage	[V]
V_{sp}	Set point voltage	[V]
V_e	Error voltage	[V]

Abbreviations

ADU	Analogue-to-Digital conversion Unit
ALE	Address Latch Enable
CE	Chip Enable
CLE	Command Latch Enable
CPLD	Complex Programmable Logic Device
DAC	Digital-to-Analogue Converter
DC	Direct Current
EEPROM	Electronically Erasable Programmable Read-Only Memory
FET	Field-Effect Transistor
fps	Frames per second
FWHM	Full-Width at Half-Maximum
FPI	Fabry-Perot Interferometer
GB	Gigabyte
I2C	Inter-Integrated Circuit
LED	Light Emitting Diode
LUN	Logical Unit
LVDS	Low Voltage Differential Signaling

MOSFET	Metal–Oxide–Semiconductor Field-Effect Transistor
NIR	Near Infrared
PCB	Printed Circuit Board
ppm	parts per million
QE	Quantum Efficiency
Q-PP-FPI	Quadrature Plate Piezo actuated Fabry-Perot Interferometer
R/B	Ready/Busy
RE	Read Enable
RGB	Red Green Blue
RH	Relative Humidity
RMS	Root-Mean-Square
UART	Universal Asynchronous Receiver Transmitter
UAV	Unmanned Aerial Vehicle
USB	Universal Serial Bus
WE	Write Enable
WP	Write Protect

1 Introduction

Spectroscopic measurements are used in a wide variety of applications ranging from satellite remote sensing to manufacturing of pharmaceutical goods. Spectral observations are used to measure electromagnetic radiation at selected wavelengths to gather data from the object. They can be used, for example, to identify different materials or to carry out accurate colour measurements. A hyperspectral imager is an imaging spectrometer that can be used to acquire a three-dimensional spectral data cube. The data cube contains two spatial dimensions and one dimension for the wavelength. Therefore, a continuous spectrum exists for each pixel in the image.

The hyperspectral imager concept used in this work uses a Fabry-Perot interferometer together with a colour image sensor to capture one, two or three wavelength bands in a single image. These wavelength bands can be extracted from the acquired raw image. The Fabry-Perot interferometer used in the imager is a tunable filter which has multiple transmission bands. Spectral data can be sampled at selected intervals by adjusting the transmission bands of sequential images. This lightweight imaging spectrometer can be used, for example, on board a UAV (Unmanned Aerial Vehicle) as part of a low cost system for spectroscopic measurements of the environment.

This work concentrates on the electrical design of the hyperspectral imager. A description of the Fabry-Perot interferometer is also given as it is one of the key components of the imager. The electronics are designed to control either one or two Fabry-Perot interferometers simultaneously. The hyperspectral imager uses a silicon based image sensor. Both monochrome and RGB versions of the sensor can be used. A flash memory is used to save the measurement data from the image sensor. The use of silicon image sensor technology allows a low cost system to be constructed but it limits the spectral range of the system to visible and very near infrared regions. The system can be tuned to other regions of the spectrum with image sensors having appropriate spectral responses.

2 Hyperspectral Imaging

A hyperspectral imager can be used to measure the spectral characteristics of the observed area. Many different instrument designs exist that are targeted for hyperspectral imaging in different regions of the spectrum. The visible light is only a small portion of the electromagnetic spectrum which is shown in Figure 2.1. The wavelength range from 200 nm to 1100 nm is suitable for hyperspectral imaging with silicon based image sensors. This wavelength range includes the UV, the visible and the very near infrared region of the spectrum.

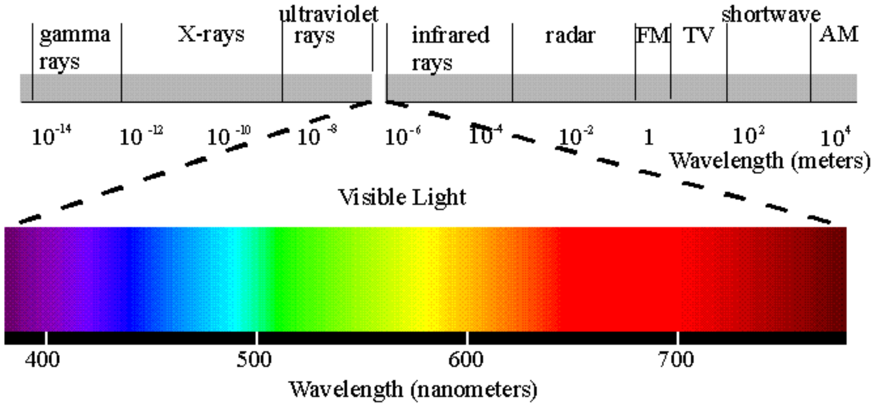

Figure 2.1. Electromagnetic radiation. Visible light is only a small part of the electromagnetic spectrum. The visible and very near infrared region of the spectrum can be observed with silicon based sensors.

A hyperspectral imager acquires spectral information on the selected wavelength bands to gather continuous spectra over the observed area. One way to acquire hyperspectral data is to take a series of images of the target with a narrow bandpass filter placed in front of a monochromatic image sensor and the centre wavelength of the filter slightly changed for each image until all the spectral bands of interest have been measured. This results in a spectral data cube which includes the spectral data for each point in the observed area. The spectral data cube can be thought of as a stacked pile of images taken of the same target. The only difference in the images is that they each contain the image information from different wavelength bands. The three-dimensional data set gathered with a hyperspectral imager is schematically shown in Figure 2.2 with the x- and y-coordinates representing the spatial dimensions and the λ-coordinate representing the wavelength.

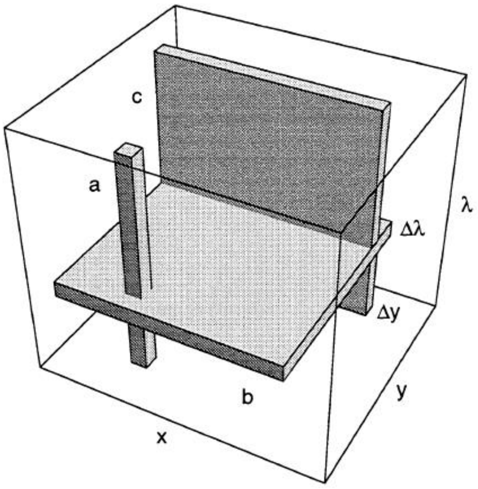

Figure 2.2. The hyperspectral data cube. Some of the possible hyperspectral data acquisition methods are also shown. Whiskbroom (a), framing camera (b) and pushbroom (c) methods can be used to gather data for a hyperspectral data cube. [1]

Figure 2.2 introduces some of the possible methods to obtain the hyperspectral data. These are (a) the whiskbroom, (b) the framing camera and (c) the pushbroom type of data acquisition. A whiskbroom instrument gathers the whole spectrum of one observed point at a time. The line of sight needs to be scanned over the target area to obtain the data for the complete data cube. The whiskbroom type of spectrometer can be realized for example with a wavelength dispersive prism and a line detector. The framing camera works in the way described earlier; One narrow spectral band is recorded from the observed area. Different spectral bands are then scanned through to acquire the whole data cube. The pushbroom type of data acquisition gathers the whole spectrum over one spatial dimension of the target at the same time. The other dimension needs to be scanned to complete the data cube. This is easily achieved for example in satellite remote sensing where the movement of the satellite relative to the Earth automatically scans the second spatial dimension. This kind of sensor can be implemented for example with a wavelength dispersive prism and an area image sensor. There are also several other ways to implement sensors that acquire hyperspectral data. [1][2]

3 The Fabry-Perot Interferometer

As the Fabry-Perot interferometer is one of the key elements in this hyperspectral imager an introduction of the component is given in this chapter. The theoretical inspection of the Fabry-Perot interferometer is mainly based on references [3] and [4]. The hyperspectral imager platform is designed to control either one or two piezo-actuated interferometer modules developed at VTT Technical Research Centre of Finland. This module is introduced at the end of this chapter.

3.1 Theory

The Fabry-Perot interferometer consists of two semi-transparent mirrors. These are placed parallel to each other with the reflective surfaces close to each other. This forms a cavity that works as an optical resonator. Constructive interference allows certain wavelengths to be transmitted through the interferometer whereas other wavelengths are reflected. The optical path length of the cavity determines the wavelengths that can be transmitted through the interferometer. If the optical cavity length is fixed the interferometer is usually called Fabry-Perot etalon and if the optical cavity length can be altered the name Fabry-Perot interferometer is used instead.

The mirrors can be made by coating optical flat substrates with a thin layer of metal such as aluminium or silver. Dielectric layers can also be used to form coatings with very high reflectance. For a high quality interferometer, the mirrors need to be flat and parallel with high precision [5]. For simplicity, in the following theoretical analysis of the Fabry-Perot interferometer the mirror plates are considered to be perfectly plane and parallel.

Both plates in Figure 3.1 are considered to have a refractive index n_1 and it is assumed that n_1 is larger than the refractive index n_2 of the medium between the mirrors. The analysis will concentrate on the reflections and transmissions at the inner surfaces of the plates and reflections and transmissions between surrounding medium and outer interfaces of the plates are not accounted for.

The electric field of an electromagnetic plane wave entering the interferometer from the left in Figure 3.1 can be written as

$$\boldsymbol{E} = E_0 e^{j(kz-\omega t)} , \tag{3.1}$$

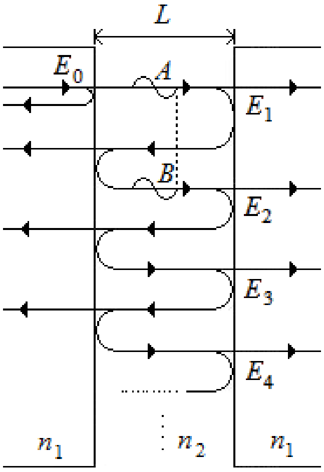

Figure 3.1. The Fabry-Perot interferometer. The path of the electromagnetic wave is shown here only for demonstration purposes. In the ideal case the wave reflects back through the same path it came from when reflected multiple times between the mirrors assuming that the wavefront is normal to the plate surface. The Figure is modified from [6].

where E_0 is the amplitude of the electric field and $kz - \omega t$ is the phase of the field. The z-axis is chosen to be normal to the plate surface. The parameter ω is the angular frequency of the wave, t is the time and the wave number k can be written as

$$k = \frac{2\pi}{\lambda}, \tag{3.2}$$

where λ is the wavelength of the light. The wave number in medium 2 between the mirrors is k_2 which is simply written as k. At the first boundary, $z = 0$, the amplitude of the electric field is E_0 and the phase is chosen to be zero. The length of the cavity is L so $z = L$ at the second mirror boundary.

The waves are reflected at the cavity surfaces with the consequence of constructive and destructive interference. Constructive interference is possible if different waves are in-phase with each other after reflections in the cavity. This is the case for the waves A and B in Figure 3.1. Transmission through the interferometer is highest for waves that interfere constructively. This is possible for the wavelengths for which the optical path length n_2L in the cavity is an integer multiple m of a half wavelength. [6]

$$m \cdot \left(\frac{\lambda}{2}\right) = n_2 L, \qquad m = 1, 2, 3 \ldots \tag{3.3}$$

where n_2 is the refractive index in the cavity which for air is $n_{\mathrm{air}} = 1{,}0003$ and is usually taken equal to 1. The parameter m is also known as a transmission order of the Fabry-Perot interferometer. The optical path length is used as the refractive medium changes the wavelength of the light compared to the wavelength in vacuum.

Light is partly transmitted and reflected at each boundary. The reflection coefficients for light coming from medium 1 to the boundary of medium 2 are written as r_{12}. The reflection coefficients for light coming from medium 2 to the boundary of medium 1 are written as r_{21}. In a similar manner the transmission coefficients are written as t_{12} and t_{21}. For light incident normal to the mirror surface the coefficients can be written as [7]

$$r_{12} = \frac{n_1 - n_2}{n_1 + n_2} \tag{3.4}$$

$$r_{21} = \frac{n_2 - n_1}{n_1 + n_2} \tag{3.5}$$

$$t_{12} = \frac{2n_1}{n_1 + n_2} \tag{3.6}$$

$$t_{21} = \frac{2n_2}{n_1 + n_2}\,. \tag{3.7}$$

If the refractive index n_1 is larger than n_2, the reflection coefficient r_{21} is negative. This can be written as a complex number $r_{21} = |r_{21}|e^{j\pi}$ which means that there is a phase shift of π radians associated with the reflections inside the cavity. Other coefficients are positive and have no phase shift associated with them in this simplified model.

The electric field entering the central medium in Figure 3.1 is $E_0\, t_{12}$ with its phase designated as 0 radians. The first electric field component $\boldsymbol{E}_1$ transmitted through both mirror plates is then

$$\boldsymbol{E}_1 = E_0 t_{12} t_{21} e^{jkL}\,. \tag{3.8}$$

In a similar way, taking multiple reflections in account, we can write for the other transmitted components

$$\boldsymbol{E}_2 = E_0 t_{12} r_{21}^2 t_{21} e^{j3kL} \tag{3.9}$$

$$\boldsymbol{E}_i = E_0 t_{12} r_{21}^{2(i-1)} t_{21} e^{j(2i-1)kL}, \tag{3.10}$$

where i = 3, 4, 5… The transmitted components can be added to get the total transmitted field $\boldsymbol{E}_t$

$$\begin{aligned} \boldsymbol{E}_t &= E_0 t_{12} t_{21} e^{jkL} + E_0 t_{12} r_{21}^2 t_{21} e^{j3kL} + \dots \\ &= E_0 t_{12} t_{21} e^{jkL} \sum_{i=0}^{\infty} r_{21}^{2i} e^{j(2kL)i} \\ &= \frac{E_0 t_{12} t_{21} e^{jkL}}{1 - r_{21}^2 e^{j2kL}}. \end{aligned} \tag{3.11}$$

From Equations 3.5 - 3.7 we can solve

$$t_{12} t_{21} = 1 - r_{21}^2 = 1 - r^2, \tag{3.12}$$

where we have designated $r = r_{21}$ [3]. The transmission function T_F of the Fabry-Perot interferometer can then be written as

$$T_F = \frac{|\boldsymbol{E}_t|^2}{|\boldsymbol{E}_0|^2} = \frac{(1-r^2)^2}{(1-r^2)^2 + 4r^2 \sin^2 kL} = \frac{1}{1 + F' \sin^2 kL}, \tag{3.13}$$

where $F' = 4r^2/(1-r^2)^2$ is the coefficient of finesse. The coefficient of finesse is high for mirrors with high reflectivity. Therefore the transmission is very small except when the term $\sin^2(kL)$ goes to zero and the transmission approaches unity. This is possible for waves that fulfill the requirements of Equation 3.3.

The simulated transmission for a Fabry-Perot interferometer is plotted in Figure 3.2 for three different mirror reflectivities. The Fabry-Perot interferometer has multiple narrow transmission bands. The transmission peak for the first transmission order, m = 1, is centered at $\lambda = 2L$ and the higher transmission orders are situated at shorter wavelengths. As the mirror reflectivity gets higher, the coefficient of finesse increases and the pass bands of the interferometer get narrower.

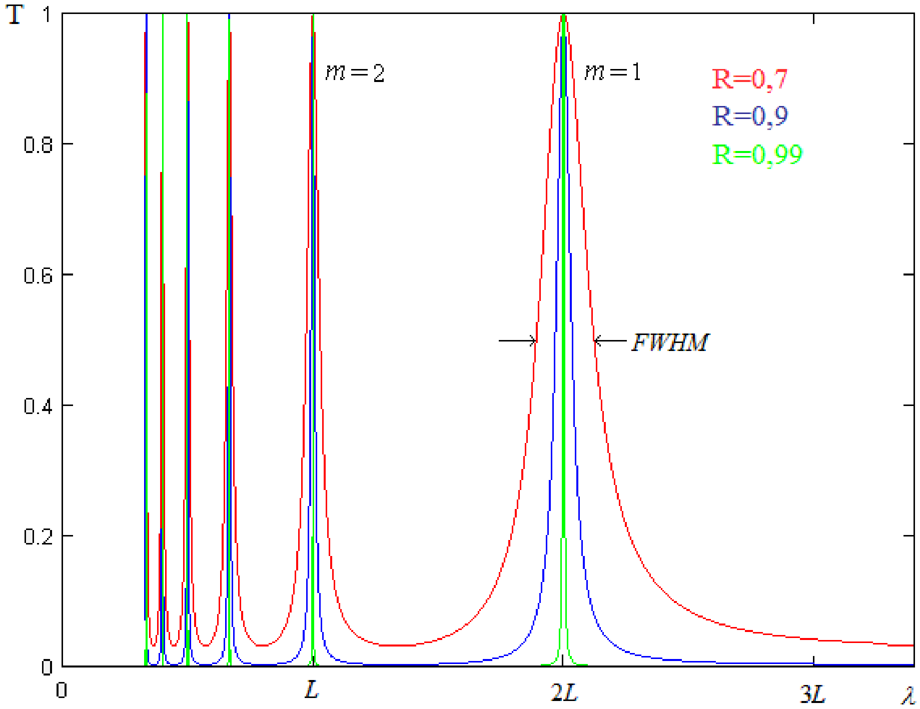

Figure 3.2. Simulated transmissions for the Fabry-Perot interferometer with three different mirror reflectivities. The full-width at half-maximum (*FWHM*) is also shown for one of the peaks.

The free spectral range, *FSR*, is the difference between two successive transmission maxima which can be expressed as

$$FSR(\nu) = \frac{c}{2nL}, \tag{3.14}$$

where c is the speed of light in vacuum [8]. When the coefficient of finesse F' is very high the full-width at half-maximum ν_{FWHM} for the transmission peak can be approximated as [8]

$$\nu_{FWHM} = \frac{c}{\pi L\sqrt{F'}}. \tag{3.15}$$

As the light is not usually perfectly normal to the mirror surface and different wavelengths may arrive in slightly different angles to the cavity, the FWHM of the transmitted wavelengths is usually somewhat wider than expected from Equation 3.15. This simplified model of a Fabry-Perot interferometer does not consider the thickness of the mirror coatings and the fact that at the reflecting surfaces the phase shift varies as a function of the incident angle. This causes a shift in the transmission maxima [9]. Absorption of the mirrors decreases the maximum transmission of the interferometer. Also, if the separation between mirrors varies spatially the performance is degraded.

3.2 Interferometer Module

The Fabry-Perot interferometers used in the designed spectrometer platform were developed at VTT Technical Research Centre of Finland as a part of the NOSPI-project (NOvel SPectroscopic technologies based on Interferometry) [10]. The Q-PP-FPI-002 Fabry-Perot interferometer module that was developed in the NOSPI-project is shown in Figure 3.3.

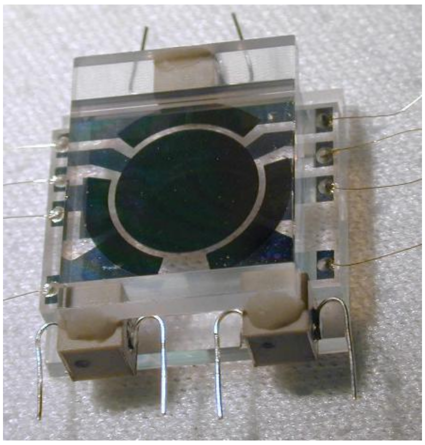

Figure 3.3. The Q-PP-FPI-002 Fabry-Perot interferometer used in the spectrometer platform is adjusted by three piezoelectric actuators. The air gap between the mirrors is measured with the electrode pairs placed near the actuators.

Layers of 5 nm Titanium, 50 nm Silver and 50 nm of SiO_2 are deposited on the substrate to form the interferometer mirrors and the measurement electrodes. The air gap between the mirrors is measured at three positions near the piezoelectric actuators which are placed at the edges of the interferometer. Each measurement capacitor consists of two capacitors connected in series. This allows a simple mechanical structure to be used as all the electrical connections for the electrodes can be made on the same mirror plate. The aperture diameter of the interferometer mirror area is 7 mm. The designed wavelength range for the Q-PP-FPI-002 module is from 400 nm to 1100 nm. A similar interferometer module has also been developed for the wavelength range from 1000 nm to 3000 nm which can be used in the short wave infrared region of the spectrum. The full-width at half-maximum has been measured to be 5 - 10 nm at the designed wavelength range for the Q-PP-FPI-002 module. The controllable air gap range for the module is from 600 nm to 3000 nm. The precise capacitance value for the measurement electrodes is not important and does not need to be known to get a value for the interferometer air gap after the calibration.

Transmission characteristics were simulated for the Q-PP-FPI-002 interferometer module during the NOSPI project. The simulation model included the shift in the transmission maxima that varies as a function of the mirror coating thickness and incident angle. Figure 3.4 shows the plotted transmission maxima for the air gap range from 600 nm to 2000 nm. It also shows how the transmission wavelengths can be adjusted by changing the interferometer air gap. Each line corresponds to a different transmission order of the Fabry-Perot interferometer.

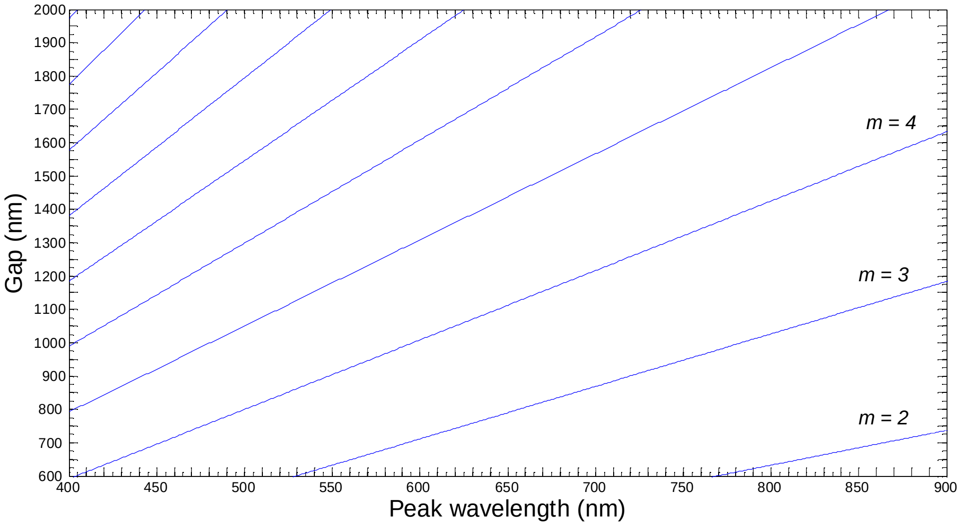

Figure 3.4. The simulated transmission maximum positions for the Q-PP-FPI-002 interferometer module in the air gap range from 600 nm to 2000 nm.

The Fabry-Perot interferometer can be used together with a band pass filter and monochrome sensor to form a hyperspectral imager for a limited wavelength range. The free spectral range of the interferometer limits the useful wavelengths for this type of instrument. The hyperspectral imager concept introduced in the next chapter utilizes multiple orders of the Fabry-Perot interferometer to expand the useful wavelength range.

4 The Hyperspectral Imager Concept

4.1 Working Principle of the Hyperspectral Imager

The key element of the hyperspectral imager used in this work is the combination of a Fabry-Perot interferometer and an RGB-image sensor [10, 11]. With this instrument it is possible to acquire 2D spatial images from one, two or three wavelength bands simultaneously. With the known spectral sensitivities of different pixels in the combination of the Fabry-Perot interferometer and RGB-image sensor, the different wavelength bands can be separated. When the air gap of the interferometer is changed, a new set of wavelengths can be acquired for the hyperspectral data cube.

Different data acquisition methods for the data cube are shown in Figure 4.1 including the method used in this work. The time required to save the hyperspectral data is reduced when several spectral bands can be recorded simultaneously. At the same time the usable wavelength range is extended substantially compared to a system which uses a monochrome sensor and only one transmission order of the Fabry-Perot interferometer.

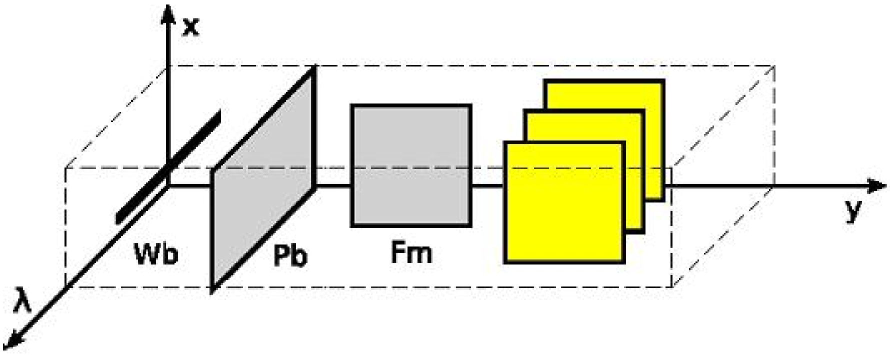

Figure 4.1 The data acquisition time is reduced when several spectral bands can be recorded simultaneously from the observed area. Figure is modified from [12].

The pixels of the RGB-image sensor are covered with a Bayer pattern filter mosaic which allows red, green and blue wavelength bands to be transmitted to separate pixels. The Bayer pattern is shown in Figure 4.2.

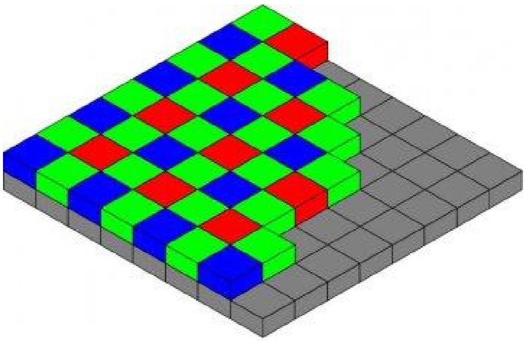

Figure 4.2. The pixels of the RGB-image sensor are covered with a filter mosaic which allows red, green and blue wavelength bands to be transmitted to underlying pixels. [13]

An MT9V022 wide-VGA colour CMOS image sensor made by Micron Technology Inc. was used in the imager [14]. The quantum efficiency (QE) is shown as a function of wavelength in Figure 4.3. The RGB-image sensor itself is already a multispectral imager that acquires data from the red, green and blue regions of the spectrum. This property of the sensor is utilized in the hyperspectral imager concept.

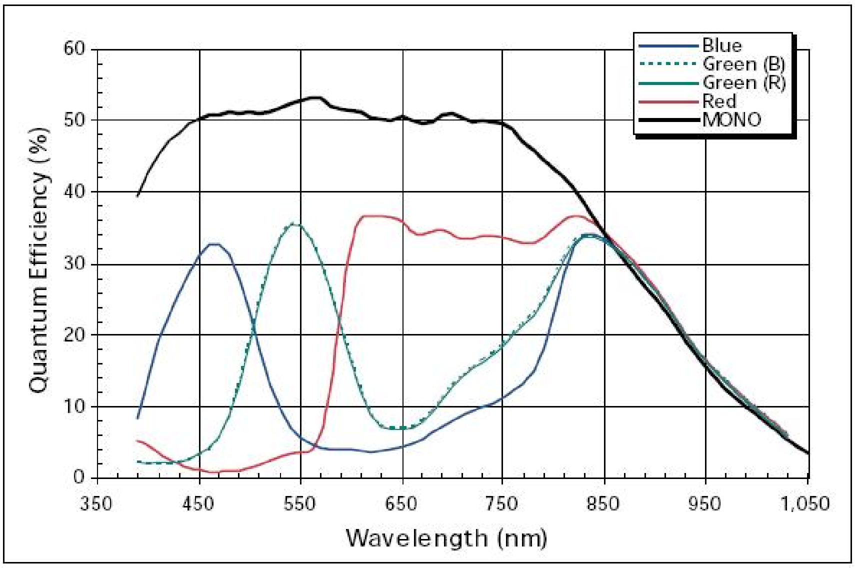

Figure 4.3. Quantum efficiency of the different sensor pixels in the MT9V022 image sensor for both RGB and monochrome versions of the sensor. [14]

The hyperspectral imager prototype built in this work can be used in the wavelength range from 500 nm to 910 nm. A silicon-based image sensor limits the wavelength range to approximately 400 nm - 950 nm. The wavelength range of the instrument is limited with high and low pass filters to cut out the unwanted transmission orders of the

Fabry-Perot interferometer. With a different set of filters other wavelength ranges can be covered. The basic concept of the hyperspectral imager is shown in Figure 4.4.

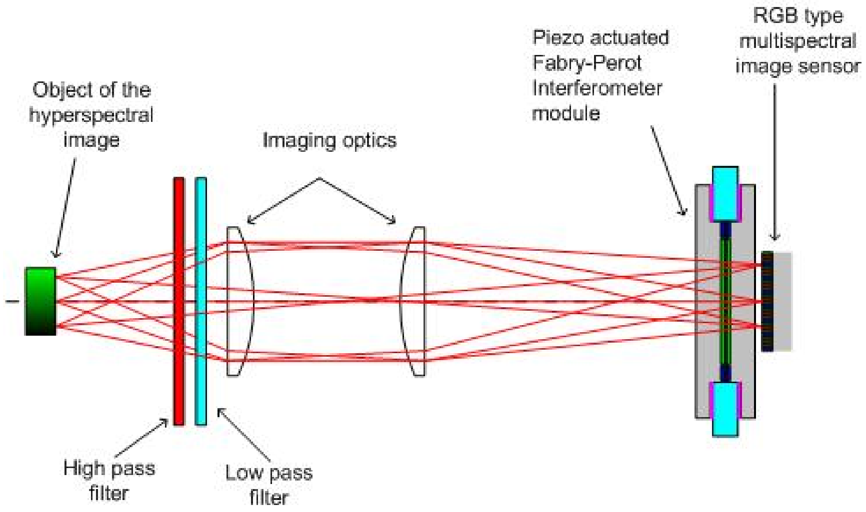

Figure 4.4. The hyperspectral imager concept. Multiple orders of a Fabry-Perot interferometer are used with an RGB-image sensor to gather the hyperspectral data. [10]

When the Fabry-Perot interferometer is placed in front of the image sensor, the sensitivity of each pixel in the interferometer-sensor module is a function of the interferometer air gap. The set of air gaps can be chosen in a way that each wavelength of interest is measured. In the calibration phase the sensitivity of each pixel needs to be measured for all the selected air gaps. These pixel sensitivities for the different air gaps can be used to solve the spectral content of the observed area. An example of the simulated sensitivities of different pixels is shown in Figure 4.5 with two different air gaps.

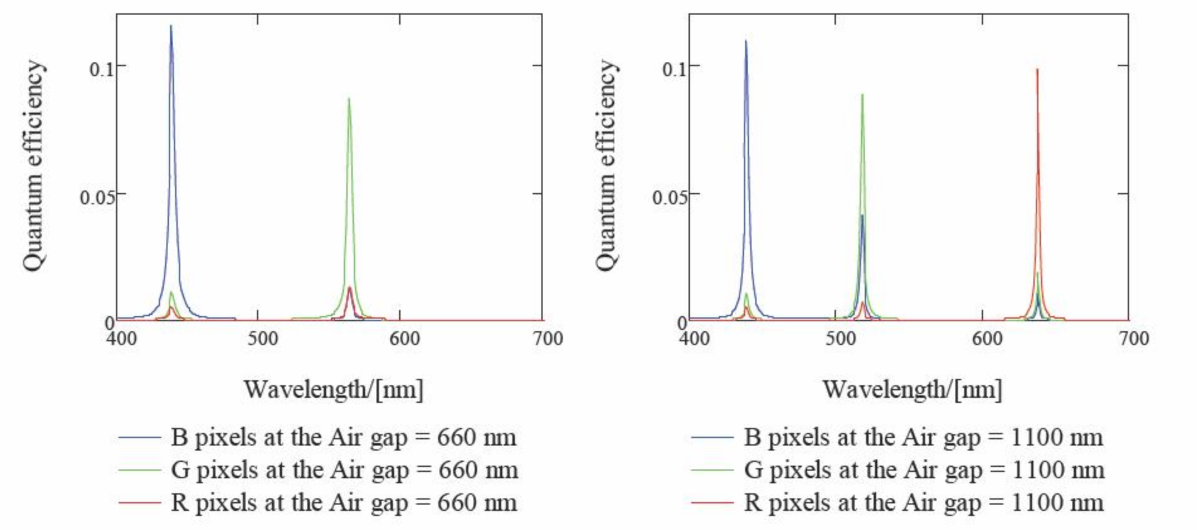

Figure 4.5. Simulated quantum efficiencies for the combination of the Fabry-Perot Interferometer and an RGB-image sensor with two different interferometer air gap values. [10]

For a certain air gap the measured pixel signals R_s, G_s and B_s can be written as

$$\begin{pmatrix} R_s \\ G_s \\ B_s \end{pmatrix} = \begin{pmatrix} S_{1R} & S_{2R} & S_{3R} \\ S_{1G} & S_{2G} & S_{3G} \\ S_{1B} & S_{2B} & S_{3B} \end{pmatrix} \begin{pmatrix} \varPhi_1 \\ \varPhi_2 \\ \varPhi_3 \end{pmatrix}, \tag{4.1}$$

where $\varPhi_{1,}$ $\varPhi_2$ and $\varPhi_3$ are the spectral photon fluxes entering the system at the different narrow transmission wavelength bands. S_{nR}, S_{nG} and S_{nB}, where n is either 1, 2 or 3, are the pixel sensitivities at the corresponding transmission bands. As the sensitivities have been calculated in the calibration phase and the measured signals are known, the spectral photon fluxes can be solved as

$$\begin{pmatrix} \varPhi_1 \\ \varPhi_2 \\ \varPhi_3 \end{pmatrix} = \begin{pmatrix} S_{1R} & S_{2R} & S_{3R} \\ S_{1G} & S_{2G} & S_{3G} \\ S_{1B} & S_{2B} & S_{3B} \end{pmatrix}^{-1} \begin{pmatrix} R_s \\ G_s \\ B_s \end{pmatrix}. \tag{4.2}$$

With the current system it is possible to save data from up to three spectral bands simultaneously in one image. After the data acquisition, the acquired images can be transformed to form the hyperspectral data cube with the help of the Equation 4.2. [10]

4.2 Requirements for the Hyperspectral Imager Platform

Several requirements were set for the hyperspectral imager in the beginning of the project. The performance requirements for the imager are shown in Table 4.1. The spectral sampling step size is defined for the second transmission order of the interferometer. This means that the central wavelength of the transmission peak changes the same amount as the air gap. Therefore this parameter can be tested directly by measuring the minimum air gap change that can be produced with the control system. Another important performance parameter of the instrument is the reproducibility of the air gap. The imager was required to be small and light weight to be applicable for handheld applications as well as for UAV-imaging purposes.

Table 4.1. Performance requirements set for the hyperspectral imager.

Parameter	**Requirement**	**Remarks**
Spectral sampling step size	< 1 nm	For second transmission order
Reproducibility of the air gap	< 0.5 nm	Over ambient temperature variations and time
Time required to change the wavelength band	< 2 ms	The time required to set the Fabry-Perot interferometer air gap to a new value
Average power consumption	< 3 W	
Maximum envelope without objective	< 110 mm x 75 mm x 55 mm	Determines the size of the imager
Mass of the instrument	< 350 g	Excluding the battery

The MT9V022 RGB-image sensor was chosen for the instrument due to its suitability for hyperspectral imaging in both visible and very near infrared regions of the spectrum. As the hyperspectral imager is intended to work autonomously during the data acquisition and, for example, to collect data onboard a UAV, a large amount of memory is needed. It was also decided that the hyperspectral imager platform should control two Fabry-Perot interferometer modules simultaneously if needed. The option for another interferometer was required to prepare the platform for different interferometer constructions that will be tested in the future. The platform is also designed to be modular in the sense that if only one Fabry-Perot interferometer is needed part of the electronics can be left out. This means that each Fabry-Perot interferometer module has its own dedicated control electronics with a simple interface to a common controller. The spectrometer control board will be responsible for the image capturing and for giving control signals to the Fabry-Perot interferometers to set the required air gaps.

5 Interferometer Control

A Fabry-Perot interferometer can be used as a tunable filter by changing the optical path length in the cavity. The parallelism between the mirrors should be controlled with high accuracy to maintain high spectral resolution. The Fabry-Perot interferometer used in this work has three piezoelectric actuators attached between the plates to control both the parallelism and the spacing of the mirrors. The control system uses three capacitive half bridges to measure the air gap. These capacitive half bridges are used to form a closed-loop control which is introduced in this chapter after a short review of previously built control systems.

5.1 Previous Control Systems

5.1.1 Pressure Control

The optical path length in the Fabry-Perot cavity can be altered by changing the gas pressure between the interferometer mirrors. This changes the refractive index of the gas and the optical path length in the cavity. Pressure can be easily controlled and it is possible to realize a linear scan of the transmitted wavelengths. An example of a spectrometer based on such a control mechanism is the PEPSIOS scanning spectrometer [15]. It has three Fabry-Perot interferometers connected optically in series. These are simultaneously scanned by controlling the pressure of each interferometer individually. Plate parallelism is maintained as the mirrors stay mechanically in the same position during the scan.

5.1.2 Piezoelectric Actuators

Piezoelectric actuators are well suited for the control of Fabry-Perot interferometers. When an electric field is applied over a piezoelectric actuator, the electric dipoles in the piezoelectric material try to align themselves parallel to this field. Mechanical stress is induced in the material which causes the actuator to change shape. Piezoelectric materials are non-conductive and are usually either crystals or ceramics. Piezoelectric actuators can be made from a single piece of material with electrodes at both ends. Another possibility is to use multilayer co-fired ceramics with electrodes embedded in the material. The multilayer structure is used to achieve higher displacements with lower voltages. [16]

The response of the piezoelectric actuators to the applied electric field is nonlinear. Another problem with the material is hysteresis. Due to these two effects it is difficult to implement an accurate open-loop control for the actuators. A closed-loop control system is more suitable as it measures the displacement of the actuator and either increases or decreases the control voltage to achieve the wanted position.

5.1.3 Optical Feedback

J.G. Winter has used piezoelectric actuators as a part of his instrument which uses three Fabry-Perot interferometers connected in series [17]. It utilizes multiloop servo control to maintain parallelism and to change the spacing of the interferometer mirrors. Each of the Fabry-Perot interferometers has three piezoelectric actuators that are adjusted according to the measured parallelism and spacing. The optical feedback system is constructed with three optical measurement channels for each interferometer. Two of them are used to measure the parallelism and one is used to measure the spacing between the plates. A reference interferometer is required for each Fabry-Perot interferometer to measure the spacing of the mirrors. The structure of the optical measurement system is shown in Figure 5.1. With the optical measurement system there is a risk that light is reflected from the control channels to the main filter area which may reduce the usability.

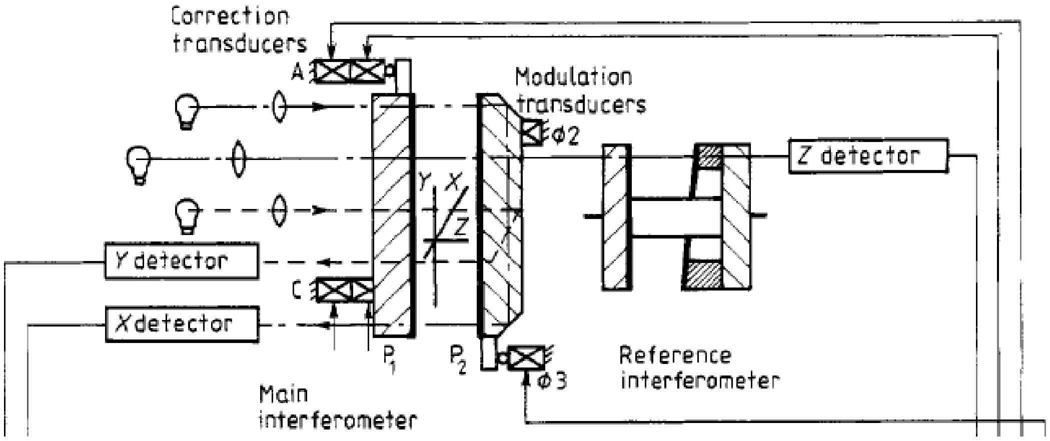

Figure 5.1. The optical measurement system used by J. G. Winter. Three optical measurement channels are used for the interferometer. Two of them are used for measuring the parallelism and one is used for measuring the spacing between the plates. A reference interferometer is required to measure the spacing of the mirrors. [17]

5.1.4 Capacitive Feedback

Another approach is to use capacitive measurement inside the closed-loop control. Such a system is described by Hicks et al. [18]. The air gap between the mirrors is measured with five sets of capacitor electrodes. Two of the capacitor electrodes are placed in such a position that it is possible to measure the parallelism in x-axis by comparing capacitance values on both sides of the interferometer. Another pair of capacitors are placed to measure the parallelism in y-axis with a similar arrangement. The fifth capacitor is used together with an external reference capacitor to measure and control the spacing of the mirrors. Parallelism and separation of the plates are controlled with three piezoelectric actuators spaced at 120° intervals around the interferometer centre. This requires an additional coordinate transformation from the measured values to control the actuators. The placement of the capacitor plates and actuators can be seen in

Figure 5.2. Spacing variations of the interferometer mirrors were measured to be less than 0.5 nm during the one hour test period with a mean plate spacing of 100 µm. [18]

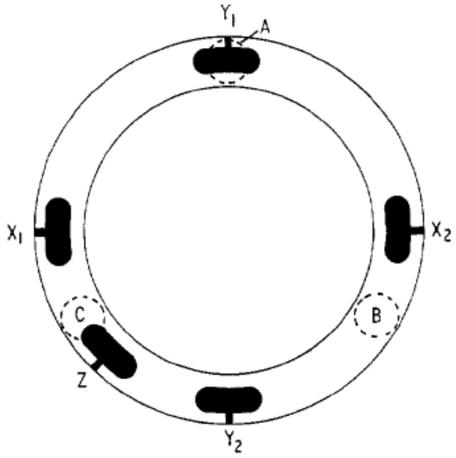

Figure 5.2. Placement of capacitor electrodes and actuators. Capacitor electrodes in positions X1, X2, Y1 and Y2 are used for measuring the parallelism of the interferometer mirrors. Capacitor electrodes in the position Z are used together with an external reference capacitor to measure the spacing of the mirrors. A, B and C are the positions of the piezoelectric actuators. [18]

Another interesting approach using capacitive micrometry has been described by Rees et al. [19]. It is quite similar to the one described above but uses only three capacitive sensing points placed close to each actuator. This approach removes the need for a coordinate transformation. Although the parallelism of the mirrors is not corrected automatically as in the system described by Hicks et al. [18], the accuracy of the capacitive measurement maintains the parallelism that is initially set.

5.2 Closed-Loop Control of the Interferometer

At this work a capacitive half bridge is used to detect deviations from the balance conditions in the air gap. The error signal from the half bridge is used by the designed closed-loop control to generate control voltages for the piezoelectric actuators to correct the measured error. The half bridge is used for measuring the changes in the capacitance rather than the absolute capacitance value. The control loop must be calibrated in order to relate the controller set point values to the air gap between the measurement electrodes.

5.2.1 Capacitive Half Bridge

A capacitive half bridge is used together with the control loop to set the air gap between the interferometer plates. The basic construction of the capacitive half bridge together with the control loop is shown in Figure 5.3.

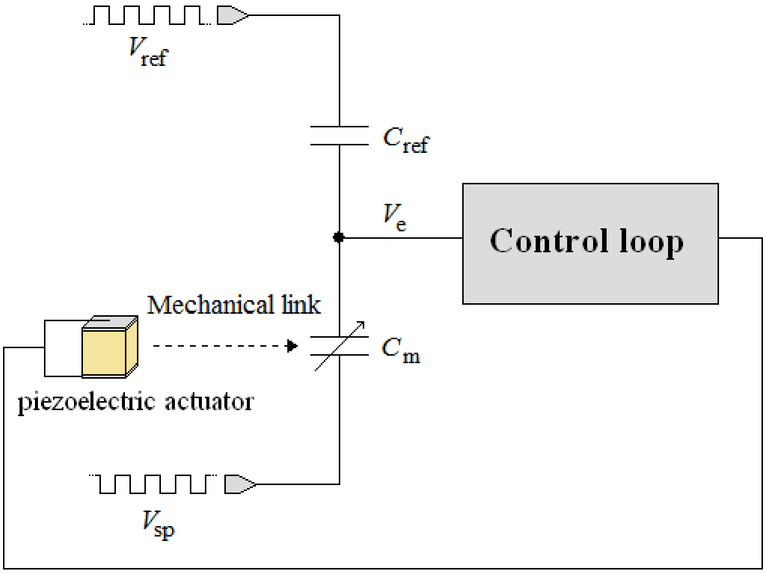

Figure 5.3. The capacitive half bridge creates an error signal V_e with amplitude proportional to the displacement from the requested air gap. The control loop is used to minimize the error signal.

The signals V_{ref} and V_{sp} are the inputs for the capacitive half bridge. The bridge consists of a reference capacitor C_{ref} and a capacitor C_{m} which is formed with the measurement electrodes in the interferometer module. The capacitance of the measurement electrodes, which were shown in Figure 3.3, can be approximated to consist of two identical capacitors C_{m1} and C_{m2} connected in series. Both of them have the same capacitance, $C_{\text{m1}} = C_{\text{m2}}$. C_{m} can be expressed as

$$C_{\text{m}} = \frac{C_{\text{m1}}}{2} = \frac{C_{\text{m2}}}{2}\,. \tag{5.1}$$

In this case C_{m1} and C_{m2} can be approximated as

$$C_{\text{m1}} = C_{\text{m2}} \approx \varepsilon_{\text{air}}\varepsilon_0 \frac{A_{\text{r}}}{d} \approx \varepsilon_0 \frac{A_{\text{r}}}{d}\,, \tag{5.2}$$

where ε_0 is the permittivity of vacuum, $\varepsilon_{\mathrm{air}}$ is the relative permittivity of air, A_{r} is the area between electrodes and d is the separation between the electrodes. The measurement capacitance C_{m} can be approximated as

$$C_{\mathrm{m}} \approx \varepsilon_0 \frac{A_{\mathrm{r}}}{2d}\,. \tag{5.3}$$

With the excitation voltages V_{ref} and V_{sp} the error signal V_{e} can be solved with the superposition principle

$$V_{\mathrm{e}} = \frac{C_{\mathrm{ref}}V_{\mathrm{ref}} + C_{\mathrm{m}}V_{\mathrm{sp}}}{C_{\mathrm{m}} + C_{\mathrm{ref}}}\,. \tag{5.4}$$

Closed-loop control is used to correct the error by driving the piezoelectric actuator into such a position that the amplitude of the error voltage V_{e} goes to zero. For this case

$$C_{\mathrm{ref}}V_{\mathrm{ref}} + C_{\mathrm{m}}V_{\mathrm{sp}} = 0\,. \tag{5.5}$$

From Equations 5.3 and 5.5 the air gap between the capacitor plates can be solved as

$$d = -\frac{A_{\mathrm{r}}\varepsilon_0}{2V_{\mathrm{ref}}C_{\mathrm{ref}}} \cdot V_{\mathrm{sp}}\,. \tag{5.6}$$

In this design V_{ref} and V_{sp} are generated as square wave signals as the square wave can be easily generated with couple of switches and the amplitude of the signal can be controlled accurately. The negative sign in Equation 5.6 is a 180° phase shift between these two signals. V_{ref} has a fixed amplitude and, therefore, the air gap between the capacitor electrodes is directly proportional to the amplitude of V_{sp}. For this reason, V_{sp} is called set point voltage as it directly sets the air gap between the electrodes through the control loop. [20]

In the ideal case, the error signal V_{e} has the same waveform as the reference and set point signals. In practice, however, there are spikes in the rising and falling edges of the error signal as the V_{ref} and V_{sp} have different rise and fall times. These are caused by the resistance in the connections of the measurement electrodes together with the capacitances C_{ref} and C_{m}.

5.2.2 Control Loop

The interferometer is controlled with a three-channel closed-loop control system. Each control loop consists of the measurement bridge, a preamplifier, a phase sensitive detector (PSD), an integrator and a high voltage amplifier which is used to drive the piezoelectric actuator of that channel. The reference signal V_{ref} is common for all three capacitive half bridges and the set point signal V_{sp} is separate for each bridge. A block diagram of one closed-loop control channel is shown in Figure 5.4.

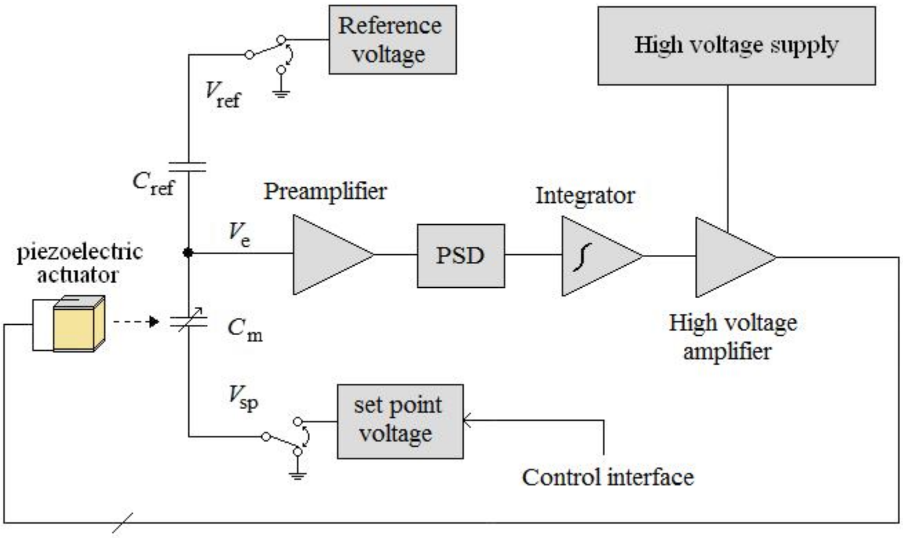

Figure 5.4. Closed-loop control and the capacitive half bridge. The control loop detects the direction of the error and drives the piezoelectric actuator to a position where the error amplitude is zero.

The phase sensitive detector is used together with the integrator to detect the direction of the error and drive the piezoelectric actuator through the high voltage amplifier. The loop is closed by the mechanical coupling between the actuator and the measurement capacitor. The air gap is driven to a position where the amplitude of the error signal goes to zero. This is the basic construction for one channel of the interferometer control loop. As one channel can be used to control the air gap between one of the measurement electrodes, a three-channel control system is required for controlling the air gap width and the parallelism between the interferometer mirrors.

6 Electronics

This chapter gives a detailed description of the electronics of the hyperspectral imager platform. A block diagram of the system is shown in Figure 6.1. The spectrometer control board can control either one or two Fabry-Perot interferometer modules simultaneously. The spectrometer control board controls the data flows from the image sensor to flash memory and from memory to a computer through a USB-interface. The control electronics of the interferometer module are first introduced in this chapter. The image sensor and the flash memory are introduced before the spectrometer control board to present the interface requirements for these external components. The PCBs (Printed Circuit Boards) and other parts of the hyperspectral imager are introduced in Appendix A.

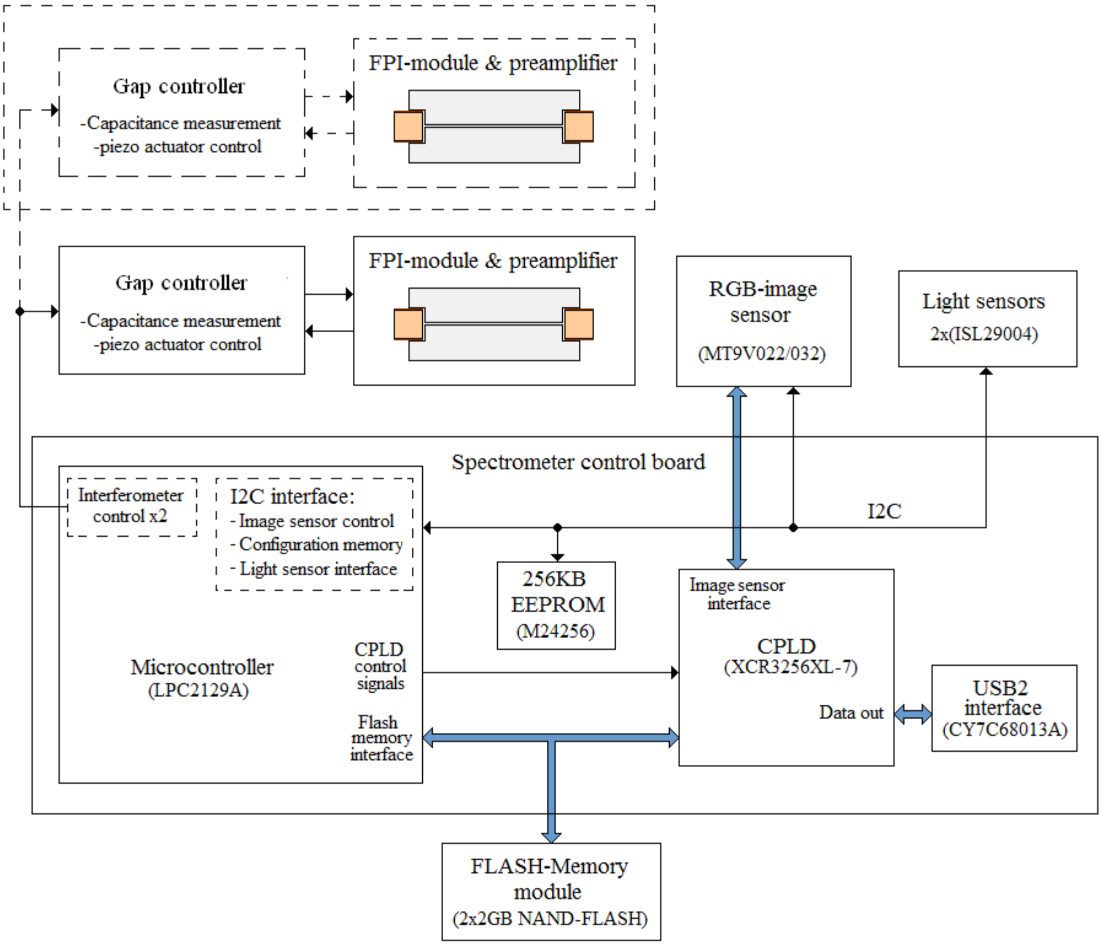

Figure 6.1. A block diagram of the hyperspectral imager. The platform can control one or two Fabry-Perot interferometer (FPI) modules simultaneously.

6.1 Interferometer Module and Preamplifier Board

The three-channel control loop for the interferometer module is based on the capacitive half bridge and the closed-loop control introduced in Chapter 5. The control loop is implemented on two different PCBs. The capacitive half bridge is placed on the preamplifier board, shown in Figure 6.2, and the rest of the control loop electronics are placed on the gap controller board. The preamplifier board is used to amplify the error signal from the capacitive half bridge and lower the impedance level before feeding the signal to the controller board.

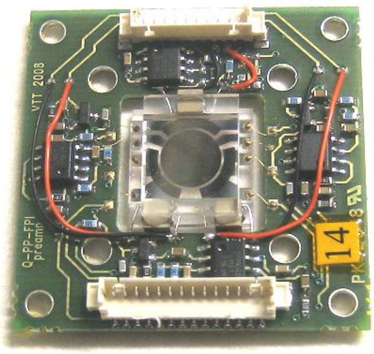

Figure 6.2. The Fabry-Perot interferometer installed on the preamplifier board. Three capacitive half bridges and preamplifiers are placed on this board.

Figure 6.3 shows the schematics of one preamplifier channel. The capacitor C1 is the 8 pF reference capacitor and the measurement electrodes of the interferometer module are connected to points CP1 and CP11 to form the capacitive half bridge.

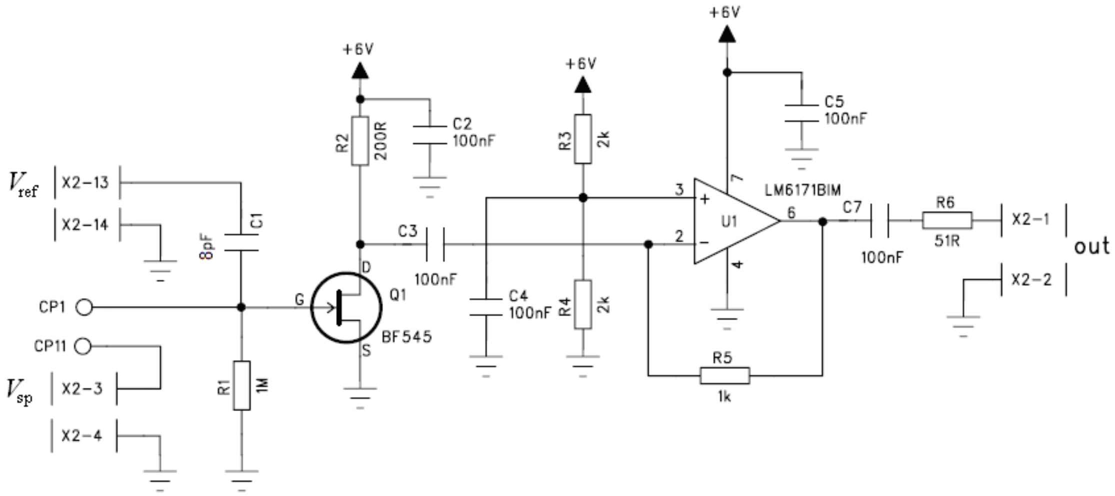

Figure 6.3. Schematic diagram of one channel of the preamplifier board that is used to amplify the error signal from the capacitive bridge.

The square wave reference voltage V_{ref} is connected to the capacitor C1 and the set point voltage V_{sp} is connected to the capacitor created by the electrodes in the interferometer module. This generates the error signal on the gate of the transistor Q1 which is a BF545 [21] n-channel silicon junction FET (Field-Effect Transistor). It is used as an impedance converter to provide a high impedance input for the preamplifier. The square wave error signal consists of a base frequency of 1 MHz and frequencies that are higher than 1 MHz. The capacitor C3 blocks the DC component from the signal and only the high frequencies are amplified. The voltage gain for the error signal in the preamplifier is approximately 3.2. The gain of the preamplifier stage drops at high frequencies which causes some distortion in the error signal.

6.2 Gap Controller

The gap controller board is used to minimize the error signal of each measurement channel by creating a three-channel closed-loop control for the interferometer module. The square wave signals for the capacitive half bridge are also generated in the gap controller board.

6.2.1 Square Wave Signals for the Capacitive Half Bridge

The gap controller board generates the square wave input signals V_{ref} and V_{sp} for each capacitive half bridge on the preamplifier board. The reference signal V_{ref} is common for all channels but the set point signal V_{sp} can be adjusted separately for each half bridge. The reference signal V_{ref} is generated with the circuit shown in Figure 6.4. The same circuit is used for generating the internal 2.5 V reference voltage for the gap controller board. The circuit Q3 is a low noise voltage reference ADR361 [22]. The reference voltage is filtered with a low pass filter and modulated to a square wave signal with a switch (ADG719) that connects the reference voltage and the ground voltage alternately to the output at 1 MHz frequency.

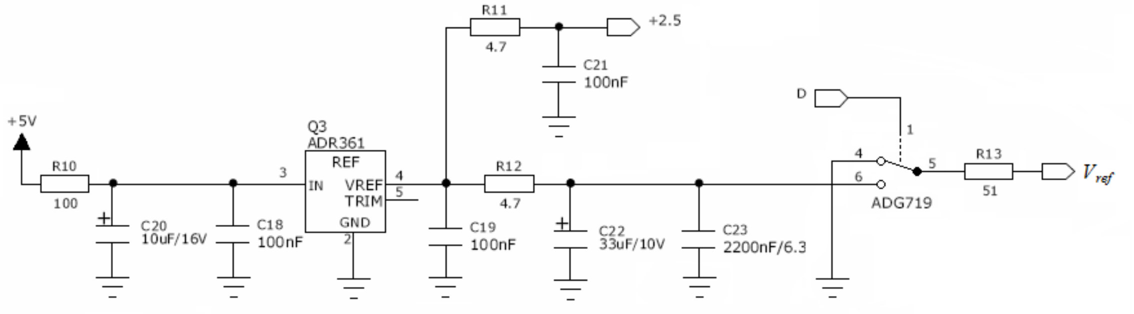

Figure 6.4. The schematics for the circuit used to generate the square wave reference voltage for the capacitive half bridge. The same circuit also generates the 2.5 V reference voltage for the gap controller board.

The circuit in Figure 6.5 is used to generate the set point voltage for one of the capacitive half bridges. The AD5662 [23] DAC (Digital-to-Analogue Converter) uses the same 2.5 V reference voltage which is used for the V_{ref} signal. The digital-to-analogue converter is used to provide a digital control interface for the amplitude of the set point signal V_{sp}. This amplitude sets the air gap between the measurement electrodes through the corresponding control loop channel.

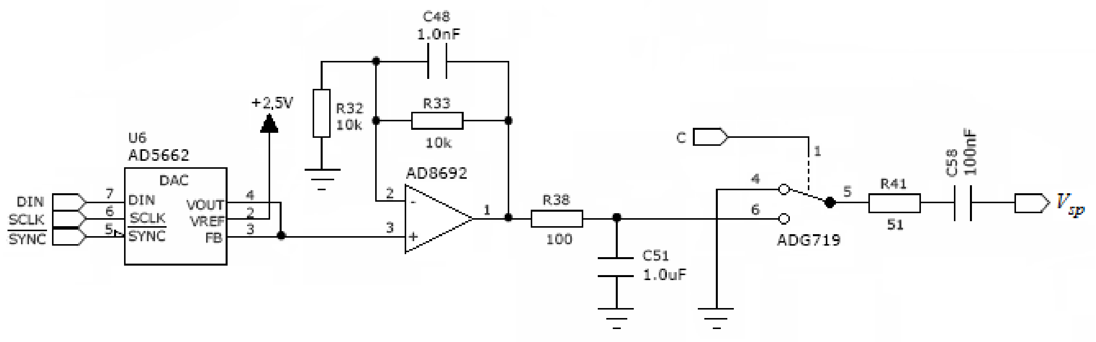

Figure 6.5. The circuit is used to generate square wave set point voltage for one of the capacitive half bridges. The control signals for the DACs are used to control the air gap of the interferometer.

The output voltage of the DAC is amplified with a gain of two in the amplifier stage. The output of the amplifier is connected to a low pass filter. If the output of the DAC is changed straight from 0 V to 2.5 V, the error signal amplitude would increase with a large step without the filter. This could cause unnecessary stress on the piezoelectric actuators. The set point voltage is modulated to a square wave with a switch (ADG719) in a similar manner as the reference voltage. As one interferometer module is controlled with three channels, three DACs are also needed on the gap controller board. The digital control interface for the interferometer is based on the control signals of these digital-to-analogue converters. The AD5662 digital-to-analogue converter needs three control signals. The SCLK signal is the serial clock input, the serial data is fed to the DIN input and the SYNC signal is used to synchronize the data transfers. All the DAC voltages are controlled simultaneously and therefore the SYNC and SCLK signals are connected to all three digital-to-analogue converters. Only the data input DIN is separate for each DAC. This reduces the number of control lines needed to control the interferometer module.

The switch control signals C and D in Figures 6.4 and 6.5 are used to modulate the V_{ref} and V_{sp} signals with a 180° phase difference. The modulation frequency for V_{ref} and V_{sp} signals is 1 MHz. The timing of the switch control signals is shown in Figure 6.6 which also shows the control signals A and B. These signals are used by the phase sensitive detector.

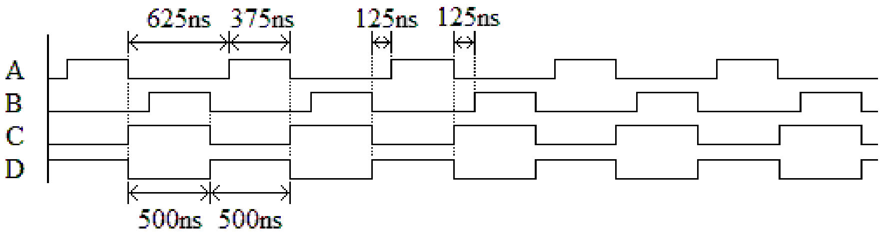

Figure 6.6. The timing of the switch control signals at the gap controller board. Signals A and B are used to control switches in the control loop to detect the polarity of the error signals and signals C and D are used to modulate V_{ref} and V_{sp} signals.

The switch control signals are created with a small AVR ATtiny24 microcontroller [24] which is shown in Figure 6.7. The microcontroller is configured to use the internal 8 MHz oscillator minimizing the number of external components. The connector J9 shown in the schematic is used for programming the microcontroller.

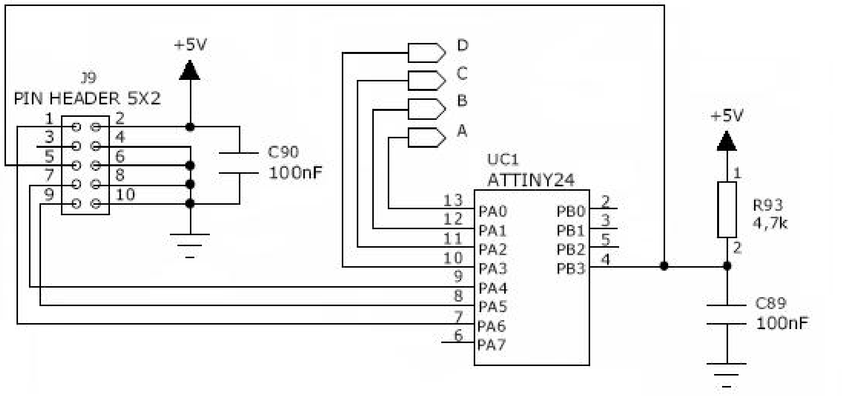

Figure 6.7. An ATtiny24 microcontroller is used to generate control signals for the different switches on the gap controller board. The microcontroller uses its internal 8 MHz oscillator.

6.2.2 Control Loop

The gap controller board takes the amplified error signals from the preamplifier board and uses these to set the control voltage for the piezoelectric actuators. Figure 6.8 shows a part of the electronics for one control channel.

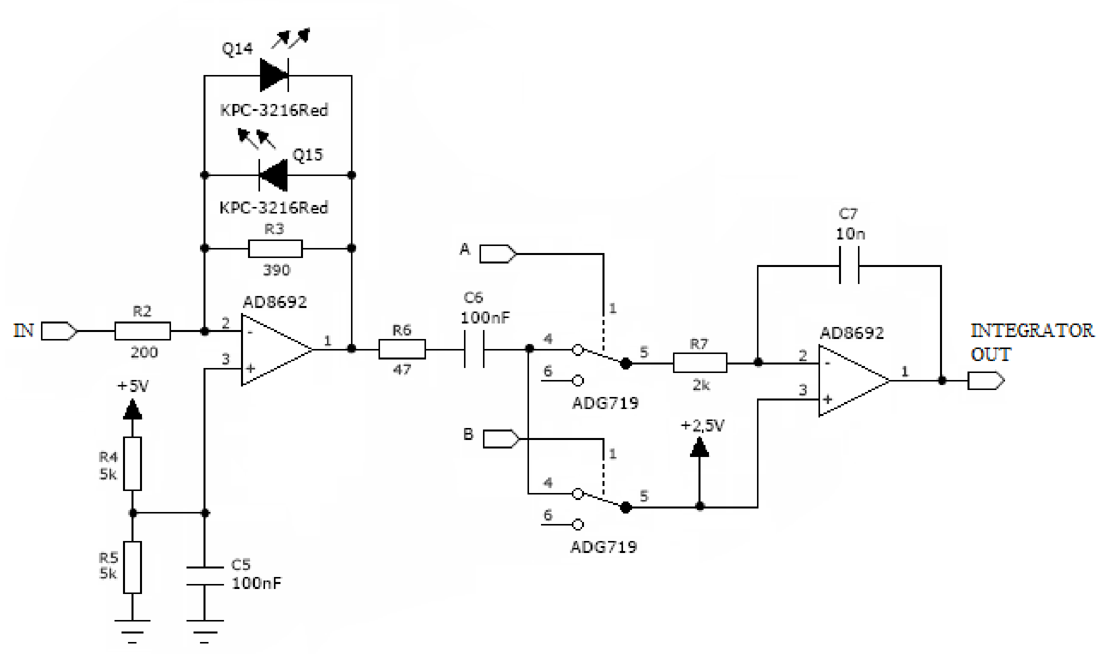

Figure 6.8. The buffer amplifier and the phase sensitive detection.

The circuit shown in Figure 6.8 contains a buffer amplifier and a phase sensitive detector. The buffer stage amplifies the error signal with a small gain of approximately -1.6. Two LEDs (Light Emitting Diodes) in the amplifier feedback are used to compress switching transients in the square wave error signal. The output of the buffer amplifier is connected to the phase sensitive detector which is based on the clamp-and-sample topology implemented using the two ADG719 switches. These switches are controlled by the signals A and B of Figure 6.6. The remaining transient spikes in the error signal are ignored by using a short time period during the spikes when neither of the switches is closed. The error signal is clamped to the 2.5 volts during the other half period and the other half period is used to integrate the error amplitude. Depending on the phase of the error signal and therefore also the error direction, the integrator output voltage either increases or decreases.

The integrator output voltage is amplified by the high voltage amplifier stage shown in Figure 6.9. The zener diode D4 is used together with the high voltage pnp-transistor Q7 and resistors R68 and R76 to create a constant current source for the circuit. A fraction of this current is flowing to the base of transistor Q6 and the rest of the current is directed to ground through the high voltage npn-transistor Q5. The ratio of these two currents can be changed with the base voltage of the Q5 transistor which is controlled by the operational amplifier. By changing the current ratio, it is possible to control the collector voltage of transistor Q5 which is also the base voltage of Q6 transistor. This voltage sets the output voltage of the high voltage amplifier. The output voltage is fed back to the operational amplifier.

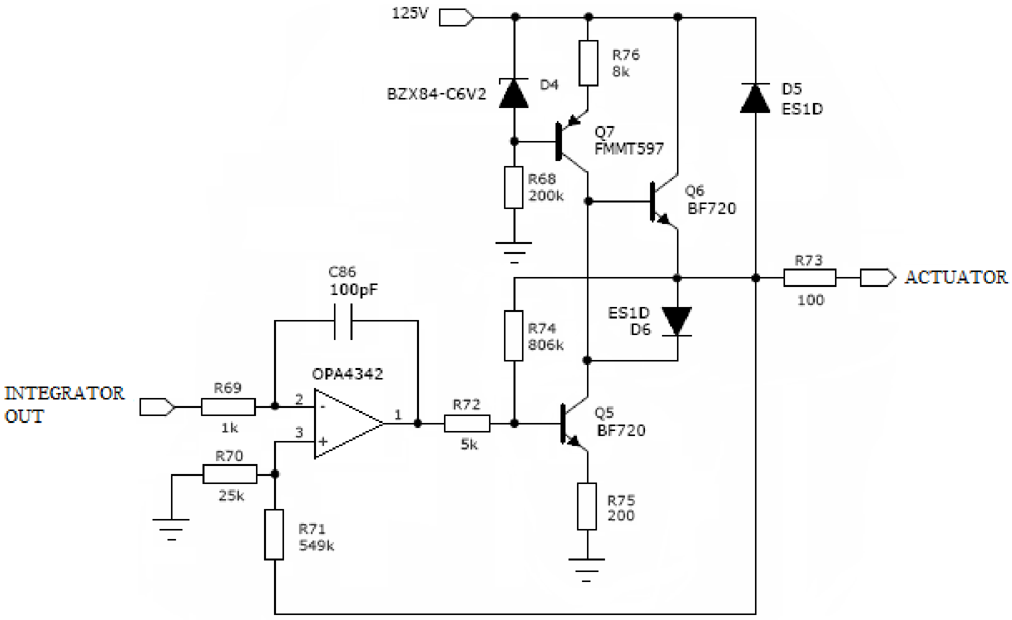

Figure 6.9. The high voltage amplifier is used to amplify the control voltage for the actuators in the closed-loop control system. There is one high voltage amplifier for each control channel on the controller board.

The amplifier drives the actuator in a direction that decreases the error signal by changing the air gap and the capacitance between the measurement electrodes. The high voltage amplifier design is a compromise between the power consumption and the interferometer settling time. The amount of current that the constant current source produces affects the speed at which the actuators can be driven. It also affects the power consumption of this stage and therefore also the total power consumption of the instrument.

The amplifier stage shown in Figure 6.9 requires a high voltage source to provide the control voltage, 0...120V, for the piezoelectric actuator. The supply voltage is generated with the circuit shown in Figure 6.10. The circuit is constructed around the MAX668 [25] step-up converter circuit. It controls the IRF7811 power MOSFET [26] (Metal–Oxide–Semiconductor Field-Effect Transistor) transistor with a 5 V pulse width modulated signal to get the output voltage to the desired level. The 5 V signal at the transistor gate allows the current to flow through the primary winding of the transformer to the ground. This stores energy in the magnetic field of the transformer. As the transistor is turned off by lowering the gate voltage to 0 V, the energy is transferred through the secondary winding of the transformer through the diode D3 to the output capacitor C30. The MAX668 DC-DC converter controls the transferred energy by changing the pulse width of the gate drive signal. The voltage divider (R55 and R57) determines the feedback voltage for the converter controller. This voltage is used to control the pulse width at the transistor gate either to increase or to decrease the output voltage. There is also an over-current protection to protect the transistor and the transformer.

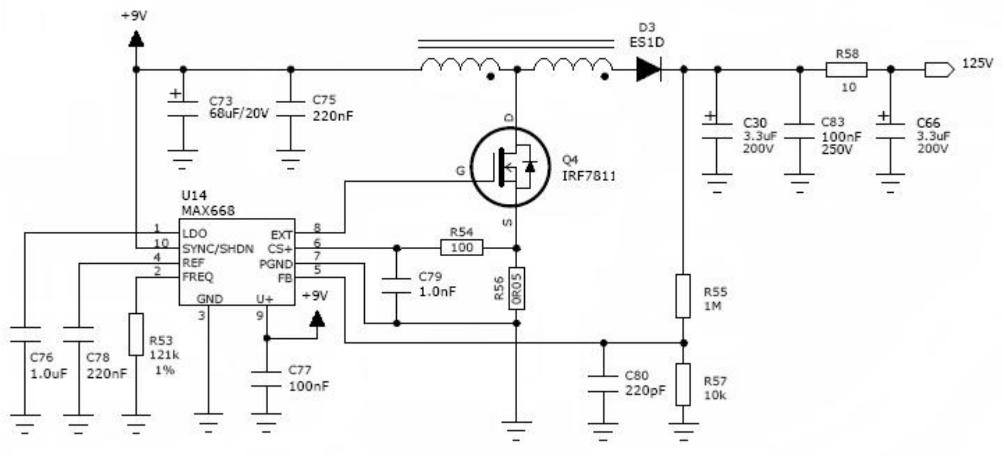

Figure 6.10. The high voltage converter is used to provide the supply voltage for the last amplifier stage of each channel. The high voltage is needed for the piezoelectric actuators.

6.3 Image Sensor

The image sensor chosen for the hyperspectral imager is the Micron MT9V022 RGB-image sensor [14]. The sensor has enhanced NIR (Near-InfraRed) performance with a quantum efficiency of over 25 % at 900 nm which makes the sensor feasible also for the hyperspectral imaging in the very near infrared region of the spectrum. Figure 6.11 shows the block diagram of the sensor. The sensor has 752 x 480 active pixels with a pixel size of 6.0 µm x 6.0 µm. The sensor can simultaneously integrate an image while the data of the previous image is read out. Therefore it is possible to achieve frame rates as high as 60 fps (frames per second) with the highest clock frequency of 26.6 MHz. An on-chip ADC provides 10 bits resolution for the pixel data of the sensor. The sensor has configuration registers for frame size, exposure time, gain and several other parameters. These registers can be configured through the two-wire I2C (Inter-Integrated Circuit) serial interface.

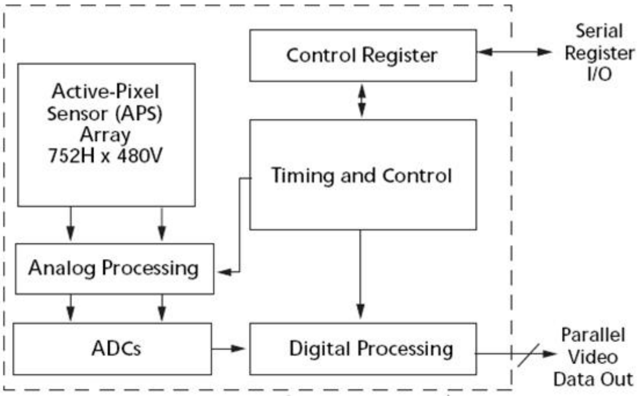

Figure 6.11. Block diagram of the MT9V022 image sensor. The Figure is modified from [14].

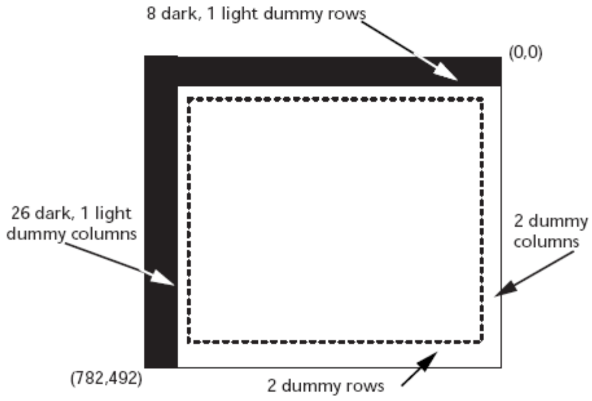

Figure 6.12. The pixel array pattern details of the MT9V022 sensor. The active sensor area is surrounded with dark and dummy pixels. [14]

Figure 6.12 shows the physical pixel array of the sensor. The active sensor area is surrounded with dark and dummy rows and columns. The dark pixels are optically black and can be used to monitor the dark signal of the sensor. The sensor is programmed to output pixels from one row at a time. It is also possible to insert blanking after each row and frame. These are called horizontal and vertical blanking which are introduced in Figure 6.13. The blanking can be used to control the time delays between rows and frames as the data is read out from the sensor.

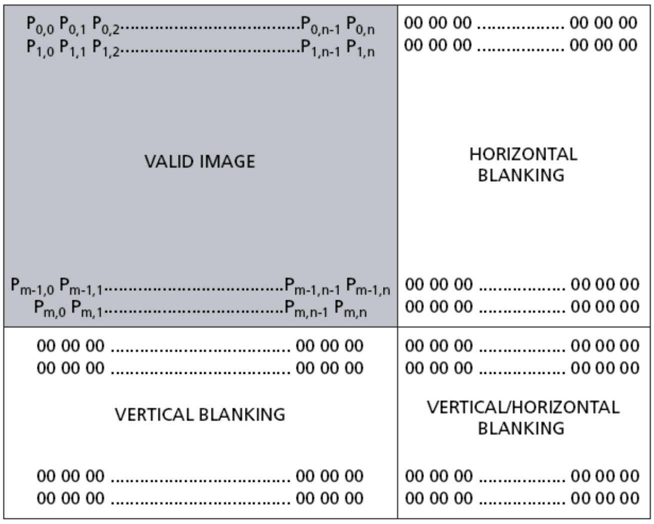

Figure 6.13. The horizontal and vertical blanking for the image sensor. Blanking can be used to control the time delays between rows and frames. [14]

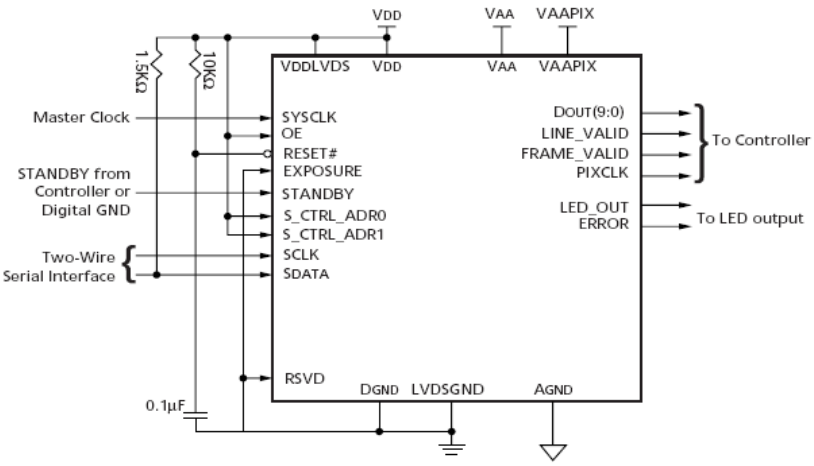

Figure 6.14. Sensor interface for parallel output mode. [14]

Figure 6.14 shows the sensor connection for parallel output mode. The Two-Wire Serial Interface is used to control the sensor parameter registers. The STANDBY signal is used to shut down the sensor to lower the power consumption and the SYSCLK is the master clock for the sensor. DOUT is the 10-bit parallel data output of the sensor which is used for the pixel data. The LINE_VALID and FRAME_VALID signals are generated by the sensor for synchronization of the data transfer. Data is valid on the rising edge of the PIXCLK signal which is derived from the SYSCLK master clock signal. Data are output as a stream of 10-bit pixel values when both the FRAME_VALID and LINE_VALID signals are high. The LINE_VALID signal is high for one row at a time. During this time pixels of one row are clocked out. Horizontal blanking determines the delay during which the LINE_VALID signal is low between rows. In a similar way the FRAME_VALID signal is high during the frame data transfer and low during the vertical blanking period. Figures 6.15 and 6.16 illustrate the timing of the interface signals.

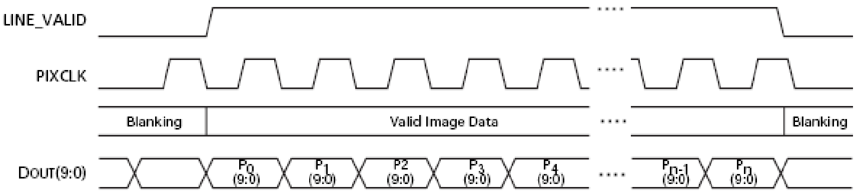

Figure 6.15. The LINE_VALID signal is high for one row at a time. During this time pixels of one row are clocked out from the sensor with the rising edge of the PIXCLK signal. [14]

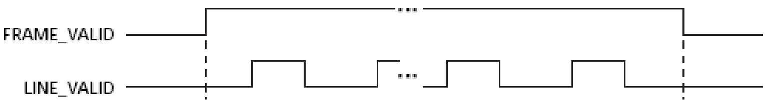

Figure 6.16. The timing between FRAME_VALID and LINE_VALID signals. The data are output as a stream of 10-bit pixel values when both FRAME_VALID and LINE_VALID signals are high. [14]

A clock frequency of 10 MHz was chosen for SYSCLK clock frequency to allow a short blanking period to be used between the rows with a frame rate of 20 fps. This leaves the system enough time to set the flash memory address during the horizontal blanking period.

6.4 Flash Memory

A large amount of memory is required for the data storage to save the images taken by the hyperspectral imager. As low mass was also a requirement a flash memory was chosen as a storage device. The timing parameters of the flash memory also complied with the requirements set by the data rate of the image sensor. The functional block diagram and the control interface for an ONFI 1.0 [28] (Open NAND Flash Interface) compliant flash memory is shown in the Figure 6.17.

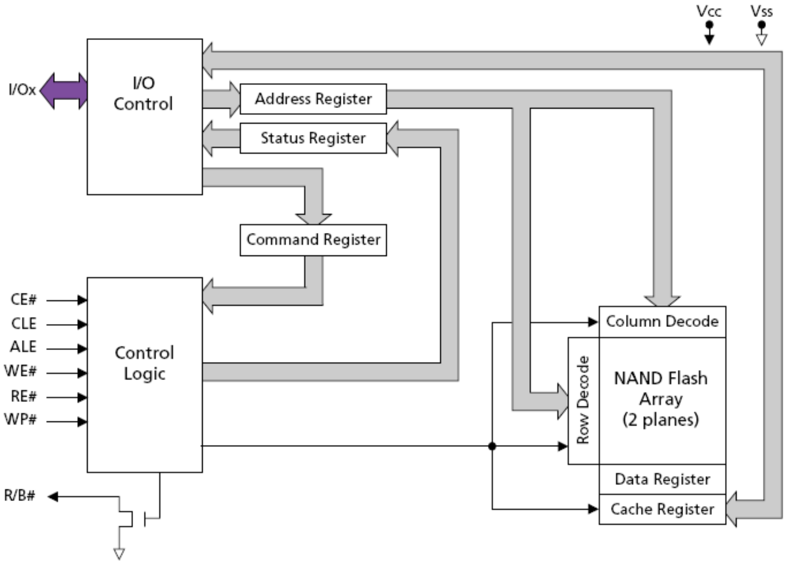

Figure 6.17. The functional block diagram and the control interface of the NAND flash memory. The memory has registers for the address, status and commands. The control logic block is used together with the command register to control the operation of the memory. [29]

The flash memory is controlled with 7 control signals and an 8-bit I/O bus. The I/O bus is multiplexed between data transfer, memory address and control commands. Commands for the Control Logic are transferred through the I/O bus on the rising edge of WE# signal (Write Enable) if the CLE (Command Latch Enable) signal is high. In the same way the memory address is transferred on the rising edge of the WE# signal if the ALE (Address Latch Enable) signal is high. The RE# (Read Enable) signal is used to clock the data out and the WP# (Write Protect) signal can be used to prevent unintentional write operations. The R/B# (Ready/Busy) signal is used for monitoring the device status. [29]

A flash memory device contains in one package one or more targets which are each selected with their own CE# (Chip Enable) signal. Each target has one or more logical units (LUNs) as shown in Figure 6.18. The logical unit is the smallest unit that can process operations independently. One logical unit has one or more page registers depending on the device used. The flash memory of one logical unit is divided into blocks each containing the same number of pages. The page size can be for example 2048 bytes or 4096 bytes depending on the device. The logical units share the same I/O bus and control lines. [28]

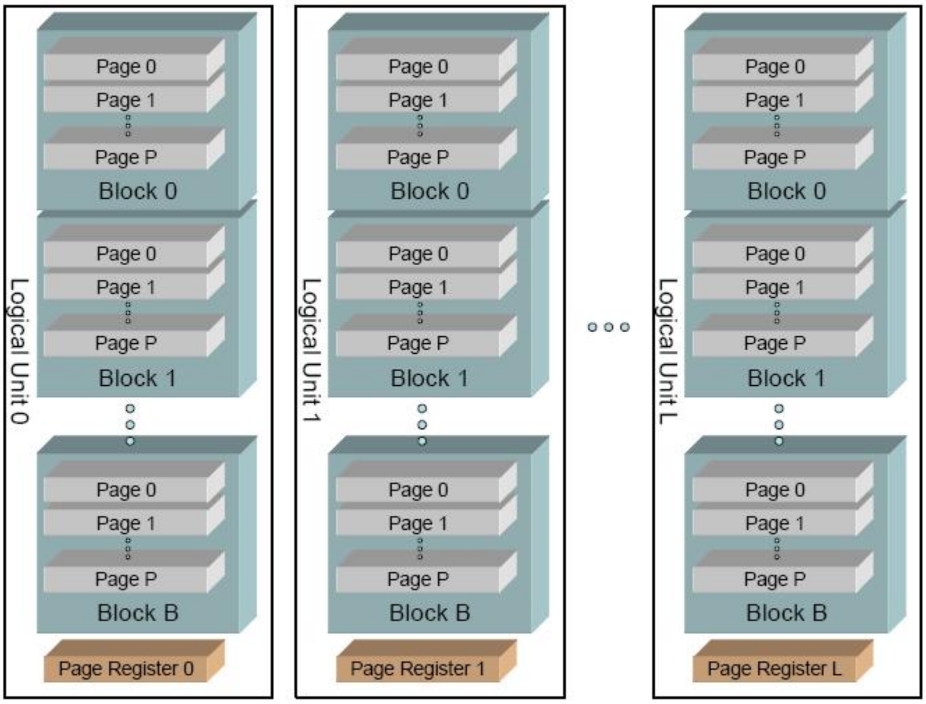

Figure 6.18. A flash memory target has one or more logical units (LUNs). Each logical unit has a page register and a memory region that is divided into blocks. [28]

Two 2 GB flash devices were assembled on the same memory bus on a small printed circuit board with a connector to form a 4 GB exchangeable memory card. The flash memory used in this work has two targets on one 2 GB flash device. Each target has two logical units with a page size of 4096 bytes.

The data saving process is initiated by writing a program page command to the flash memory. This is followed by a five byte address written to inform the memory where the following data will be saved. After this, the data is clocked into the page register one byte at a time. When the page register holds the data, another command is sent to initiate the write process. The worst case programming time for moving one full page register to the flash memory is 700 µs [28]. The architecture of the flash memory used in this work allows the data to be written on both page registers of the target before the programming is initiated. The programming time is the same as it would be for programming only one page. Figure 6.19 shows the data saving sequence for simultaneous two-page programming.

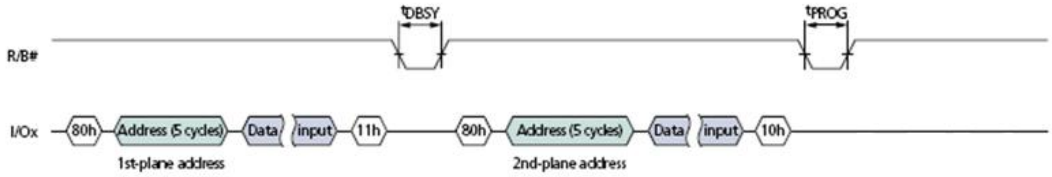

Figure 6.19. The flash memory write sequence for two-page programming mode. [29]

The 80h command byte initiates the programming mode which is followed by the 5 byte address. After the data is written to the first page register a dummy program command byte 11h is given. A similar write sequence is then generated for the second page register. After the data is written to the second page register a command byte 10h is given to initiate the write process. Programming takes place during t_{PROG}. The CE2# signal can be used to select the second target in the device. This section of flash memory contains its own set of registers but the I/O bus and the control signals are shared with the other target. There are four page registers to be used in a single flash device. Part of the data can be written to the page registers in the target selected with the CE# signal. Then the programming phase is started. While this memory region is busy, data can be written to the second target selected with the CE2# signal. The image data is thus interleaved in these two memory regions.

6.5 Spectrometer Control Board

The main function of the spectrometer control board is to control the air gap of one or two interferometer modules and save the data from the image sensor. The main components in the spectrometer control board are the LPC2129A ARM7 microcontroller from NXP [30] and the XCR3256XL CPLD (Complex Programmable Logic Device) [31] from Xilinx. These two are used together to create the necessary interfaces for the interferometer modules, image sensor and flash memory. A high speed USB 2.0 interface is implemented with QuickUSB design created by Bitwise Systems [32] to transfer data from the flash memory to a computer.

A part of the design for the spectrometer control board is from electronics previously developed at VTT. These include the microcontroller, the USB interface, the image sensor connections and the 256 kB EEPROM-memory (Electronically Erasable Programmable Read-Only Memory) connected to the I2C-data bus. The CPLD circuit is also from previously designed electronics but both the digital logic design and the physical connections to the microcontroller were completely redesigned by the author to provide the support for the external flash memory. Part of the program code was also rewritten to support the flash memory interface and the operations needed during the image capturing.

The CPLD is a programmable logic device which is used to provide the necessary glue logic and data handling between the image sensor and the flash memory. In a similar way, the CPLD circuit is used to provide the necessary interface between the flash memory and the USB interface chip. The CPLD circuit cannot provide all the functions which are required for these interfaces. Therefore the microcontroller is used to control the different data paths on the CPLD circuit. It also controls the image sensor, flash memory addressing, interferometer modules, gathers additional data from the external light sensors and generates metadata for the captured images. It also interprets the commands given by the user.

6.5.1 Transferring Image Data to Flash Memory

As the pixels of the image sensor are in 10-bit format and the flash memory data bus is only 8 bits wide, data conversion is needed before saving the data in the flash memory. A simple method is to divide the 10-bit data into two bytes. This would leave over 37 % of the memory space unused. A more efficient method is used to convert the data format. The CPLD takes the data of three successive pixels which is 30 bits and adds two zero bits in the end. These 32 bits are then saved as four 8-bit values in the memory. Table 6.1 illustrates the repartitioning of the data.

Table 6.1. The 10-bit pixel data is converted for the 8-bit data bus of the flash memory by combining the data from three successive pixels to four bytes.

pixel	0										1										2										x	x
bit	0	1	2	3	4	5	6	7	8	9	10	11	12	13	14	15	16	17	18	19	20	21	22	23	24	25	26	27	28	29	30	31
byte	0								1								2								3							

Figure 6.20 shows the logic designed for the CPLD that provides the data repartitioning functionality. The 10-bit pixel data is brought from the image sensor to the logic where three successive pixels are latched in three 10-bit D flip-flops. These 30 bits are connected to a multiplexer that selects one of the four data bytes to the output. The multiplexer state is changed sequentially to output each byte. LatchOutGen is a logic block which uses the same 10 MHz clock signal as the image sensor to generate control signals for the data repartitioning logic. The same block also generates the write enable signal for the flash memory.

Four rows of image data can be saved in the flash memory page with a size of 4096 bytes. This would make a total of 4 × 752 × (4/3) bytes ≈ 4010.7 bytes with 752 pixels per row. This value was later changed to 762 pixels per row to simplify the data repartitioning logic. An even number of 4064 bytes is then needed by the four rows of image data which is easier to process in the CPLD. The additional pixels are the black pixels from the start of each row shown in Figure 6.12.

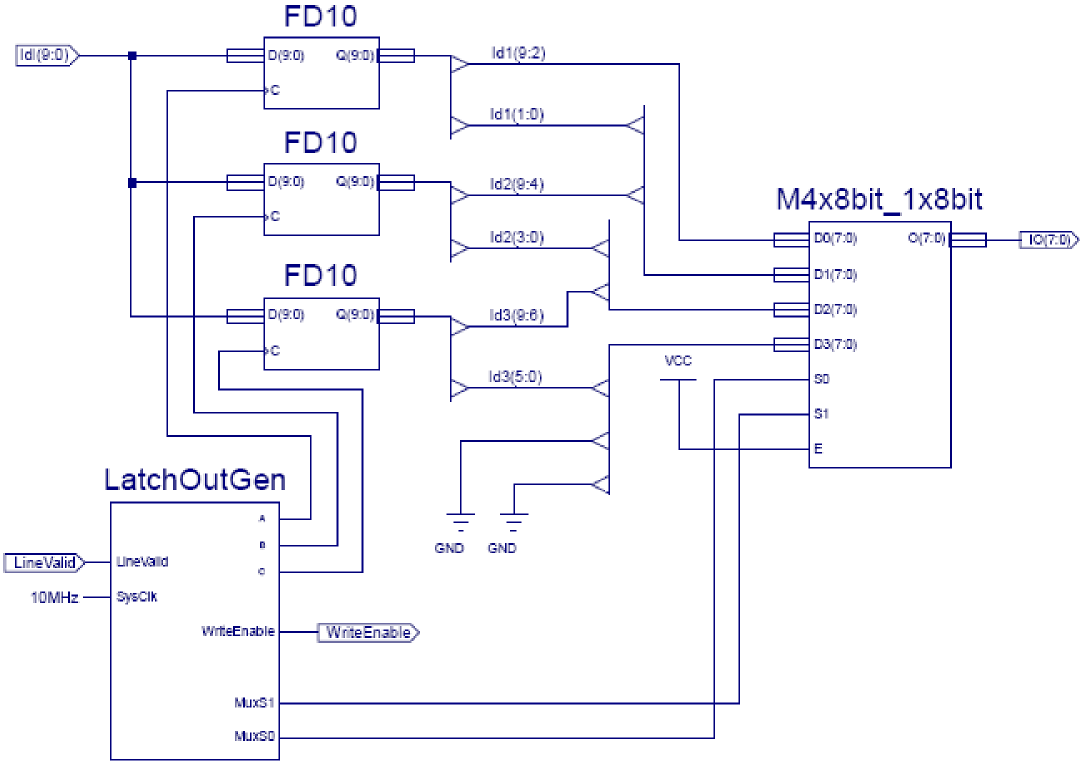

Figure 6.20. The data repartitioning block. The data of three successive pixels is latched in D flip-flops and multiplexed to the output as four bytes. The LatchOutGen block controls the timing of the D flip-flops and the multiplexer.

The image sensor data is clocked out one row at a time. After each row there is a short adjustable blanking period. This leaves time for the microcontroller to write a new flash memory address when the page register is full. For maximum data rate the blanking period should be as short as possible. On the other hand, the blanking period should be long enough to leave adequate time period for changing the flash address. As the data is clocked out from the image sensor with a 10 MHz clock signal, one pixel is clocked out each 100 ns. The data of one row, 762 pixels, requires 76.2 µs to be written in the flash page register. Without the blanking period, eight rows of data would take 609.6 µs to be clocked out from the sensor. When inserting a blanking period of 11.3 µs after each row, it takes 700 µs to write the data of 8 image rows in two page registers. This is the maximum specified time that it takes to program the data of two page registers in the flash memory. Therefore, this is also the minimum horizontal blanking period that can be used if the data is interleaved to different memory regions with CE# and CE2# signals. It takes approximately 10 µs for the controller to write a new flash memory address and send the necessary commands to save the data after every four image rows. With these settings, the data of 480 image rows is saved in the memory in 42 ms. After each frame, the microcontroller saves additional metadata which contains the flash address for the frame, air gap information, integration time, time stamp and the values from the two light sensors. This metadata is saved in the page following the last row of the image. With the metadata the achieved frame rate for the imager is 20 frames per second.

Most of the flash memory control signals are driven by the microcontroller. These include the CE# and CE2# signals for flash memories as well as ALE, CLE and WP# signals. The microcontroller can also select which R/B# signals are connected through the CPLD. When the microcontroller writes a new address for the flash memory or writes metadata, it needs to control the WE# signal (Write Enable) of the flash memory. The CPLD also needs the ability to control the WE# signal when saving the image data to the memory. The logic shown in Figure 6.21 gives the microcontroller the ability to select the source of the WE# signal.

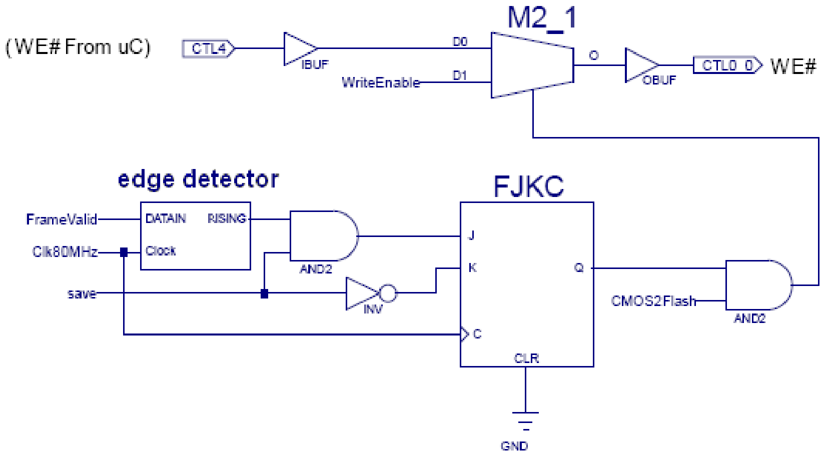

Figure 6.21. The WE# signal can be controlled by the microcontroller when writing commands, address or metadata. The control of the WE# signal can be handed over to the CPLD when the image data is transferred to the memory.

The microcontroller controls the WE# signal when image data is not written to the flash memory. When the microcontroller detects a trigger signal, it writes the appropriate commands and address for the memory and asserts the CMOS2Flash and save signals high. The edge detector logic block detects the rising edge of the FrameValid signal which changes the state of the JK flip-flop. This changes the state of the multiplexer and the control of WE# signal is given for the logic shown in Figure 6.20. The image data is moved to the flash page register with the write enable signal generated by the LatchOutGen logic block. The Line valid signal is used by the CPLD to detect when four rows of image data are moved to the memory. This means that the page register is full and a new address needs to be written for the flash device. The CPLD informs the microcontroller that four rows of data are moved to memory and the microcontroller asserts the CMOS2Flash signal low which allows the microcontroller to regain control of the WE# signal. When the new address is ready, the CMOS2Flash signal is set high and the CPLD is given the control of the WE# signal.

Table 6.2 shows how the data are organized in the 4 GB flash memory card. The data of two frames are interleaved in the memory region of four blocks. A total of 8191 frames can be saved in the memory.

Table 6.2. Four memory blocks are used for two frames and each frame is interleaved in the memory region of the two targets controlled with the CE# and CE2# signals.

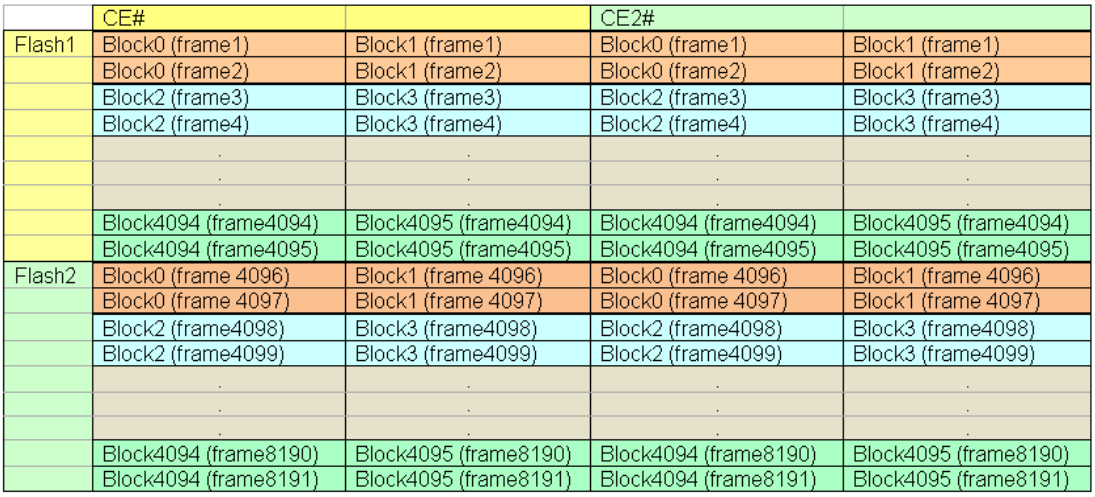

	CE#		CE2#	
Flash1	Block0 (frame1)	Block1 (frame1)	Block0 (frame1)	Block1 (frame1)
	Block0 (frame2)	Block1 (frame2)	Block0 (frame2)	Block1 (frame2)
	Block2 (frame3)	Block3 (frame3)	Block2 (frame3)	Block3 (frame3)
	Block2 (frame4)	Block3 (frame4)	Block2 (frame4)	Block3 (frame4)
	.	.	.	.
	.	.	.	.
	.	.	.	.
	Block4094 (frame4094)	Block4095 (frame4094)	Block4094 (frame4094)	Block4095 (frame4094)
	Block4094 (frame4095)	Block4095 (frame4095)	Block4094 (frame4095)	Block4095 (frame4095)
Flash2	Block0 (frame 4096)	Block1 (frame 4096)	Block0 (frame 4096)	Block1 (frame 4096)
	Block0 (frame 4097)	Block1 (frame 4097)	Block0 (frame 4097)	Block1 (frame 4097)
	Block2 (frame4098)	Block3 (frame4098)	Block2 (frame4098)	Block3 (frame4098)
	Block2 (frame4099)	Block3 (frame4099)	Block2 (frame4099)	Block3 (frame4099)
	.	.	.	.
	.	.	.	.
	.	.	.	.
	Block4094 (frame8190)	Block4095 (frame8190)	Block4094 (frame8190)	Block4095 (frame8190)
	Block4094 (frame8191)	Block4095 (frame8191)	Block4094 (frame8191)	Block4095 (frame8191)

6.5.2 Transferring Data to Computer

Image data are transferred from the flash memory to a computer through the high speed USB 2.0 interface. The USB interface is implemented with Bitwise Systems QuickUSB design. The QuickUSB design is based on the Cypress CY7C68013A microcontroller that provides several ports which can be controlled through the USB interface. The USB interface uses the UART (Universal Asynchronous Receiver Transmitter) port to send commands from the computer to the LPC2129A microcontroller. The 8-bit parallel ports A, B and D are connected to the CPLD. Port A is a general purpose I/O port which is used for handshaking between the computer and the spectrometer control board while uploading images to the computer. The handshaking is used to inform the microcontroller when the data of one memory page is read and the new address needs to be written. Ports B and D can be used for 16-bit high speed parallel data transfer between the imager memory and CY7C68013A microcontroller. The microcontroller sends the data through the USB port to a computer. At the computer the data is repartitioned into 10-bit pixel data.

Figure 6.22 shows a timing diagram for the data transfer with the QuickUSB simple I/O mode [26]. For this mode, only the IFCLK, REN and nOE control lines of the QuickUSB circuitry are needed in addition to the 8-bit parallel data connections. The UART port is used to send a command to the microcontroller to initiate the data transfer. The microcontroller writes the address for the flash memory and informs the computer that the memory is ready for the data transfer. The control is transferred from the microcontroller to the CPLD and the transfer can start.

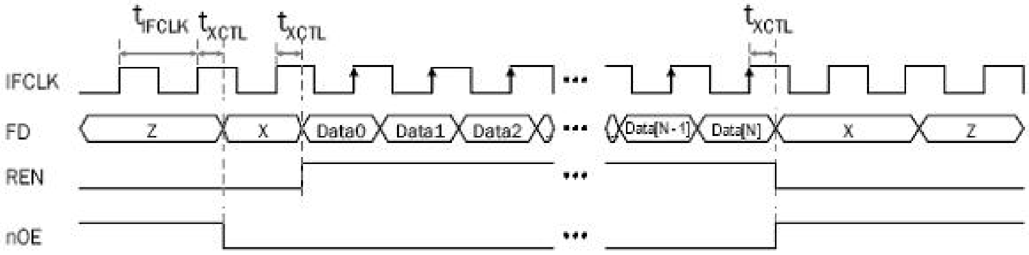

Figure 6.22. Timing diagram for the QuickUSB data transfer. Figure is modified from [26].

Figure 6.23 shows the interface logic in the CPLD for the USB data transfer. In normal operation, the microcontroller has the control of the flash RE# signal. When the computer requests data from certain address in the memory, the microcontroller sets the flash memory address and changes the state of Flash2USB high. This signal is also connected to port A to inform the computer that the memory is ready. When the computer initiates the transfer the nOE signal goes low and the REN signal goes high. These signals are connected to a three input AND port to provide the control signal for the multiplexer. When data are transferred from the memory to a computer, the IFCLK signal controls the RE# signal of the flash memory. The IFCLK signal is a 20 MHz clock signal generated in the CPLD. When one page of data is transferred, the computer informs the microcontroller through port A that the transfer is ready. Then the microcontroller asserts the Flash2USB signal low and writes the next address for the flash memory. The same transfer sequence is repeated until the whole image is transferred to the computer. After this, the computer may request another image to be transferred if necessary.

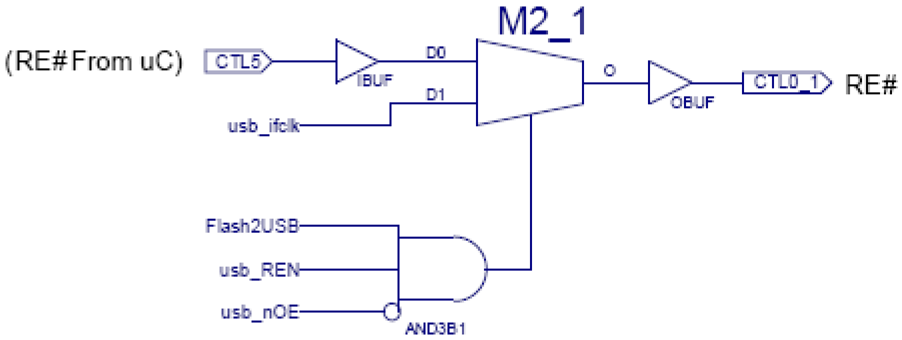

Figure 6.23. The RE# signal for the flash memory can be controlled by the microcontroller or by the USB 2.0 interface circuitry when transferring data from the memory to the computer.

7 Control Software

This chapter introduces the hyperspectral camera control program. The program runs on the microcontroller of the spectrometer control board. The microcontroller is used to control the interferometer modules. It can change the image sensor parameters, write data to flash memory and control data flow from the image sensor to the memory and from the memory to an external computer. It can also write and read data from the EEPROM-memory connected to the I2C data bus which is used for saving parameters and interferometer air gap control values. The program code includes many functions which can be used from the external computer. These functions can be initiated by giving commands to the microcontroller through the QuickUSB UART connection.

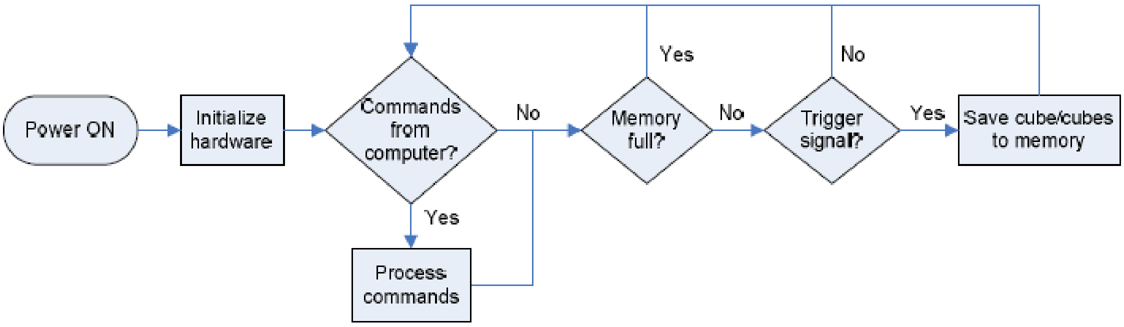

Figure 7.1. The hyperspectral imager program flow. The program polls the trigger signal and commands from the computer. If there is free space in the memory, the trigger signal initiates the data acquisition for the data cube.

Figure 7.1 shows the main program flow on the microcontroller. At start up the image sensor is initialized by the microcontroller. The initializing parameters include the image size, blanking periods, exposure time and the frame capturing mode. The frame capturing mode is set to continuous to get the highest possible frame rate for the system. This means that the image sensor is capturing frames all the time but the data is ignored until the microcontroller initiates the data transfer from the sensor to the memory. After that, the pre-programmed air gap table is loaded from the EEPROM-memory to the data memory of the microcontroller. This table includes the set point values for the three control channels of the gap controller board which are used to control the interferometer air gap. The program checks if the computer has given any commands for the system that need to be processed. After this, the program checks the address counter to see if the memory is already full. If the memory is full, the program only polls for commands from the computer until the data from the flash memory are transferred to the computer. If there is free space in the memory, the trigger signal is also polled until one arrives. This starts one of the subroutines that changes the air gap of the interferometer module by sending the control values from the air gap table. After the exposure, the next air gap is set and the data from the previous image are transferred to the memory during the new exposure. The same procedure is repeated for each air gap value in the table. If the user has given the system a command to save more than one data cube with one trigger signal, the same procedure is repeated as many times as requested.

7.1 User Program Functions

The user has control over the following camera parameters and functions:

- Integration time
- Number of raw cubes taken with one trigger signal
- Time delay between cubes if several cubes are taken with one trigger signal
- Erase two images from the flash memory
- Erase the entire flash memory
- Erase memory for one cube from the end of the memory and save a cube
- Trigger the camera
- Change the air gap table values in the EEPROM-memory
- Read one image from the memory

The user must change the integration time parameter according to the lighting conditions. The user can also acquire more than one data cube with one trigger signal. This is useful, for example, onboard a UAV where the imager can be set to acquire data during the entire flight with only one trigger signal given before takeoff. With the 20 fps data acquisition rate, data can be stored in the 4 GB memory for 7 minutes if the data are recorded continuously. An adjustable time delay can be used to adjust a delay between consecutive data cubes. The user can erase the memory with a minimum of two images at a time. In most cases the user acquires the needed data, uploads them to a computer for processing and erases the whole memory for the next data acquisition. It is also possible to change the memory card and continue data collection before the data are uploaded to a computer. One of the functions can be used to erase space from the end of the memory and save one data cube to this space. This is mainly used for finding the most suitable integration time before the data acquisition. The camera can be triggered with a push-button, a trigger pulse with amplitude between 3.3 V and 5 V or with a trigger command from the computer. The user can select the wavelengths which are acquired for the spectrum by rewriting the air gap set point values in the EEPROM-memory. The user can also upload the raw images from the flash memory to the computer.

8 Measurements

This chapter presents the measurements that were made to provide more information of the system performance. The spectral sampling step size was tested by measuring the interferometer air gap change for the smallest step in the control values. The noise in the preamplifier stage output was also measured in order to estimate the noise induced air gap movement. The reproducibility of the air gap was measured in three different tests: In the first test the interferometer temperature drift was measured in a climate chamber to see how the interferometer air gap changes as a function of the temperature. In the second test the air gap of the interferometer module was kept in the same position for a 48 hour period to measure the drift. The drift in the interferometer air gap was also measured in an endurance test where one of the interferometer modules was driven continuously between two different air gap values between February and October 2009. The settling time of the air gap was measured for a 200 nm step change. The average power consumption, the size and the mass of the hyperspectral imager were also measured. The measured interferometer air gap values are only indicative and the actual air gap might be slightly different due to the measurement method. The air gap is estimated by comparing simulated transmission spectra with different air gap values to the measured transmission spectrum. Cross-correlation and interpolation is used to find the air gap which gives the best match for the measured spectrum. The absolute value of the air gap is not important as the hyperspectral imager is calibrated with a monochromator which sets an accurate wavelength scale for the instrument. However, the air gap measurement method is well suited for measuring drift and other changes in the air gap.

8.1 Spectral Sampling Step Size

The spectral sampling step size was tested by changing the air gap with the smallest step possible and by measuring the average air gap before and after the step. Average values are used due to variation in the measurement results. The difference between the measured average values gives the smallest step size for the interferometer air gap. The smallest step in the air gap was measured to be 0.2 nm.

8.2 Preamplifier Noise

The noise of the preamplifier stage is important as the control loop considers the noise in the error signal as an error in the interferometer air gap. The control loop corrects this error by changing the air gap which causes a small random movement in the mirrors. The noise was measured at the preamplifier output with a Hewlett Packard 89410A Vector signal analyzer. The RMS (Root-Mean-Square) noise voltage was measured to be 217 µV in the frequency range from 10 kHz to 10 MHz. From this value the equivalent air gap change was estimated to be 0.1 nm. This is the worst case estimation as most of the noise occurs at frequencies filtered out by the control loop. The analysis made for the noise induced air gap fluctuation is shown in Appendix B.

8.3 Air Gap Reproducibility

8.3.1 Temperature Characteristics

The temperature characteristics of the interferometer module and the control electronics were measured in a climate chamber. The first test was done with the interferometer module and preamplifier board in the chamber with the control electronics placed outside at room temperature. The altered temperature affected only the interferometer module and the electronics of the preamplifier board. In the second test the whole control system was placed inside the chamber. In both tests the air gap between the interferometer mirrors was measured at three different positions at different temperatures. Three optical fibres were connected in a mount in front of the interferometer module and a light source was connected to the other side of the interferometer. Figure 8.1 shows the measurement setup without the light source.

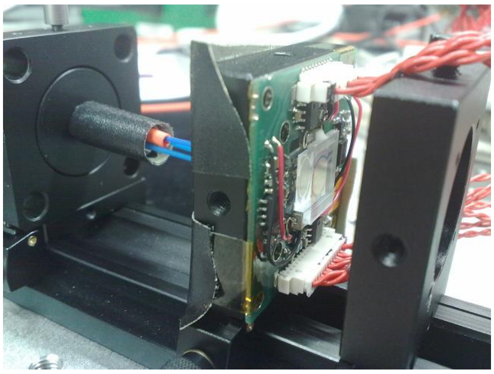

Figure 8.1. The interferometer air gap was measured at three different positions in a climate chamber. The transmission spectrum of each point was acquired by changing the fiber to a spectrometer.

The measurement fibres were connected one at a time to an SM200 spectrometer from Spectral Products to measure the transmission spectrum at the corresponding measurement point. The acquired transmission spectra were used to estimate the air gap values at these measurement points. Figure 8.2 shows the results for the first test where only the preamplifier board and the interferometer module were in the chamber. The temperature was adjusted with 5°C steps from 10°C to 30°C and back to 10°C. The temperature probe of the climate chamber did not measure the temperature from the position of the interferometer. Therefore a separate temperature measurement was made by using a second temperature probe which was placed near the interferometer. The largest temperature drift, approximately 0.5 nm/°C, was measured for channel 1. Figure 8.3 shows the measured results for the second test in which all the control electronics were placed in the climate chamber together with the interferometer.

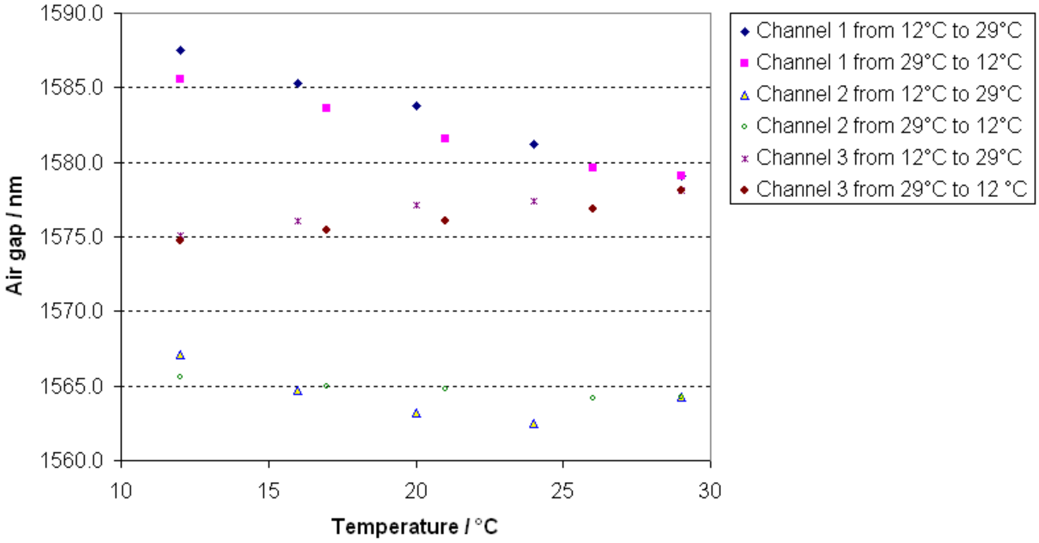

Figure 8.2. The air gap of the interferometer was measured at three positions at different temperatures. The temperature was varied from 12°C to 29°C. Only the interferometer and the preamplifier board were placed in the climate chamber.

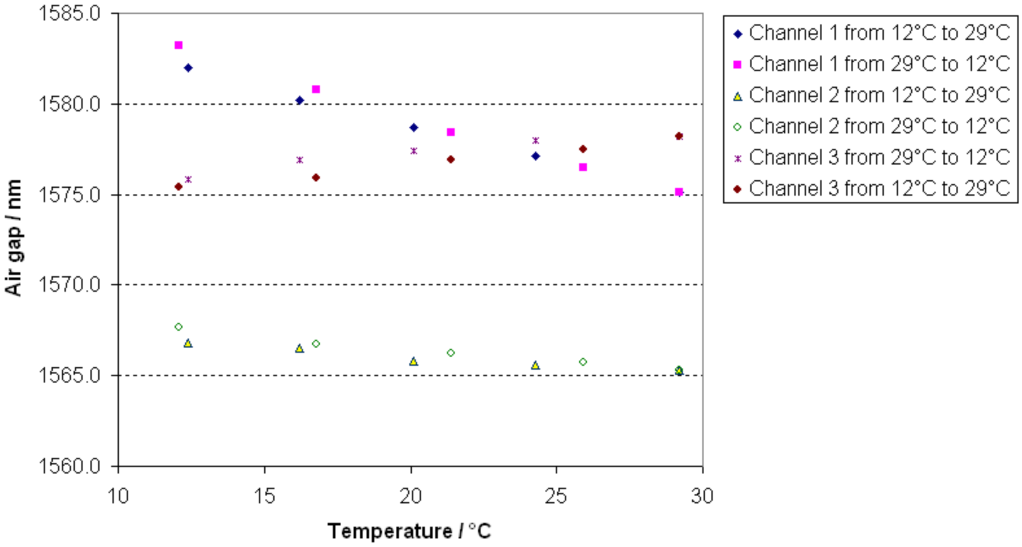

Figure 8.3. The test was repeated with all the control electronics placed in the climate chamber. The largest temperature drift was approx. 0.5 nm/°C for measurement channel 1.

The initial air gap values had changed between the tests. The biggest change in the measured air gap was 5 nm in channel 1. The measurement fibres were bent to get the control electronics in the climate chamber for the second test. The air gap of the interferometer was slightly curved which causes the measured air gap to change when the measurement place changes. The most interesting result from the test is the positive air gap change with increasing temperature in measurement channel 3. This is different from the negative slopes of the other two channels. Temperature changes may cause strain in the mirrors as the thermal expansion of the mirror substrate and actuators are different. Therefore the mirrors may deform and cause the air gap to change in a different way in different positions. It is also possible that the capacitance of the reference capacitors drifts in different directions. According to the manufacturer the temperature coefficient of the capacitance of the reference capacitors is ±30 ppm/°C. This could also cause the effects seen in the measurement. However, the capacitance change is probably not the only cause for the drift. The parasitic series resistance of the measurement capacitors also change with the temperature. High quality capacitors with small drift parameters should be used to minimize the drift.

8.3.2 Drift Tests

A 48 hour drift test was carried out for one of the interferometer modules. The air gap set points were kept constant during the test. The air gap and the interferometer temperature were measured during the test. Figure 8.4 shows the measured values. The measured air gap RMS value varies approximately 0.1 nm in a short measurement period. The RMS noise of the measurement system is approximately 0.05 nm. In the 48 hour period the air gap drifts approximately 0.6 nm which is partly explained by the change in room temperature.

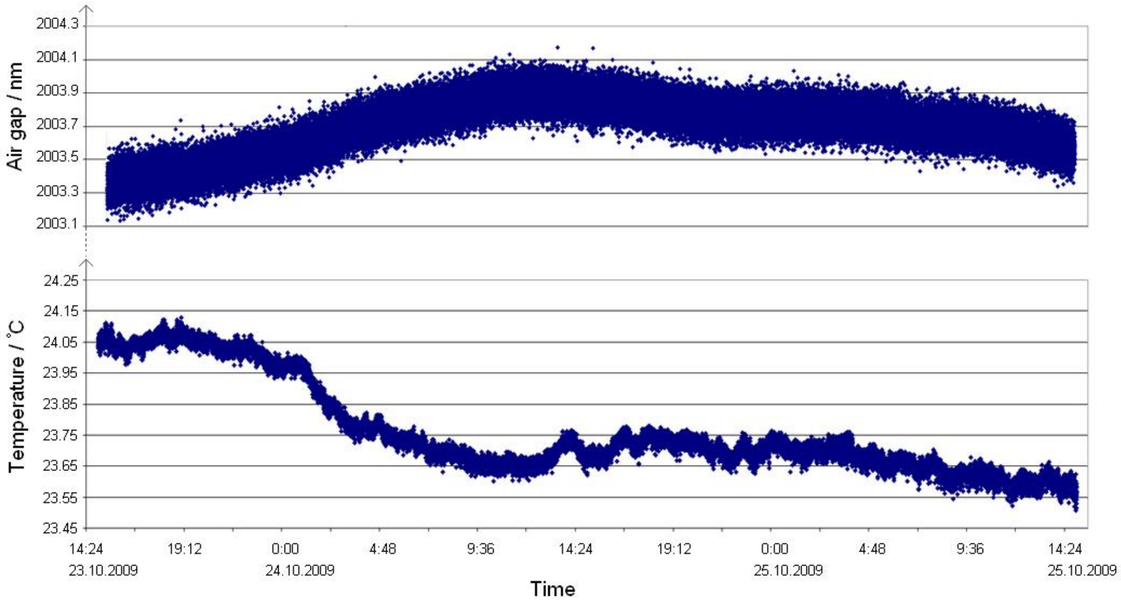

Figure 8.4. A 48 hour drift test was made for one of the interferometer modules.

Another interferometer module was placed in an endurance test in February 2009 to see how the air gap would change during a long time period. The interferometer was programmed to change the air gap between 2000 nm and 2100 nm at frequency of 100 Hz. During the eight-month test period the interferometer air gap was changed over four billion times. The frequency was temporarily set to 0.1 Hz for each air gap measurement. Measured values for both air gaps are shown in Figure 8.5.

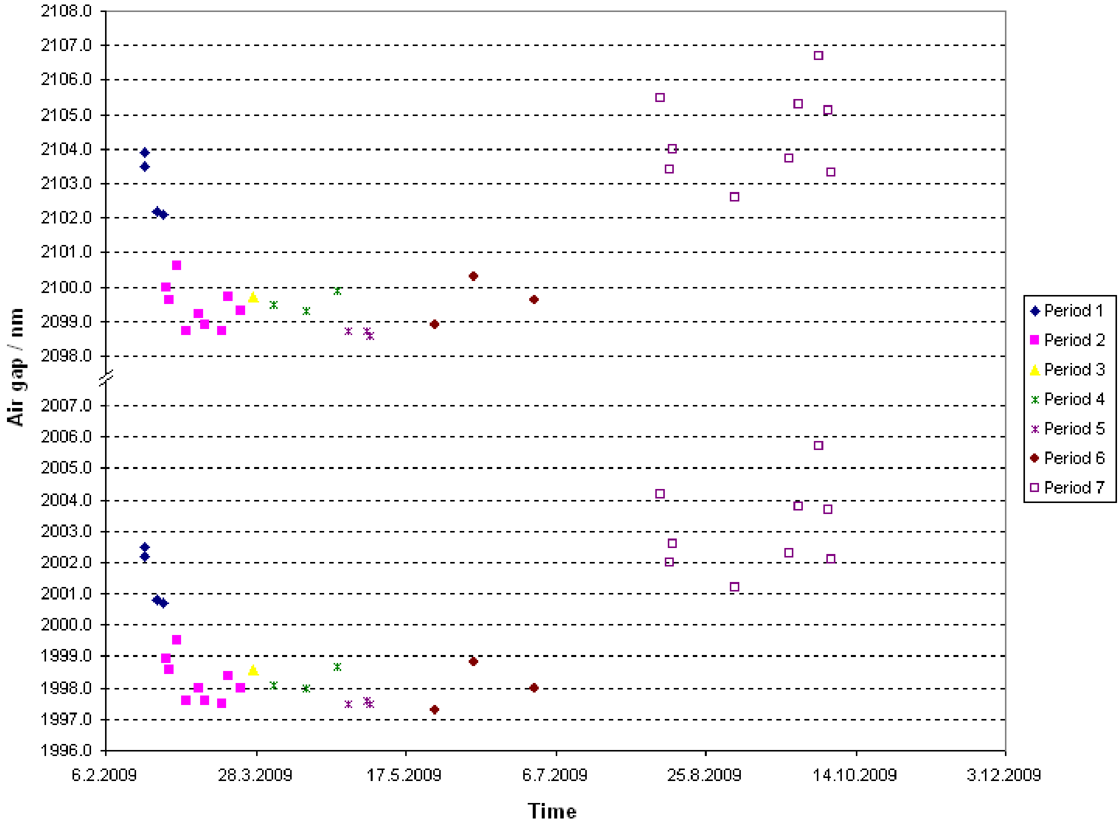

Figure 8.5. The measured air gap value for the air gap settings of 2000 nm and 2100 nm. Results are divided into different time periods as the measurement position might have changed between the measurements.

A couple of problems were detected during the test. The interferometer module chosen for this potentially destructive test was one with the air gap varying spatially by more than 40 nm over the 7 mm diameter aperture area. This module could not be used in a hyperspectral imager due to the poor planarity of the mirrors. As the same light source and measurement fibre were used in calibration measurements for the other interferometer modules as well, the measurement position varies between the measurements. An apparent step change is possible in the measured air gap if the measurement point is changed. Therefore, the measurement results have been divided into different periods during which the setup was not altered. The test was momentarily interrupted due to a power failure during the summer. This was noticed after a week and the test was continued. After the first week’s burn-in period the measured air gap drifted by less than 1 nm from the average position for both set points during the first four months. After this period the measured values show an increase in the variation. The step change in the measured air gaps after July is probably caused by a change in the measurement position.

Figure 8.6 shows the room temperature which was recorded together with each air gap measurement. The temperature is one of the factors that have an effect on the measured air gap variation. The cause of the increased variation is not known at the time of writing. One possibility is that the multilayer piezoelectric actuators are slowly losing their integrity. Similar tests should be carried out for several modules to get more samples for further analysis.

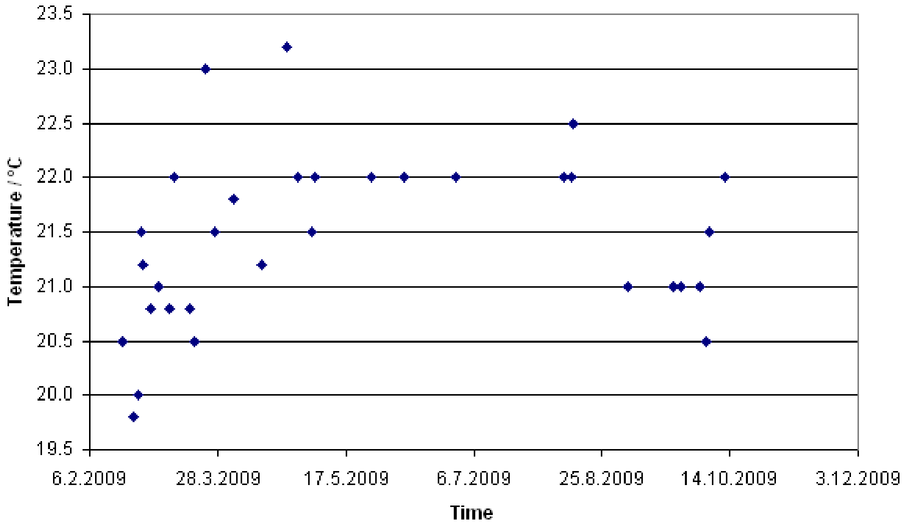

Figure 8.6. Room temperature during the air gap measurements.

The difference between the two different air gaps was also calculated for each measurement. These results are shown in Figure 8.7. During the whole eight-month test period the largest variation was 0.3 nm from the average difference of 101.3 nm. This means that both air gap values have drifted in the same direction between the measurements.

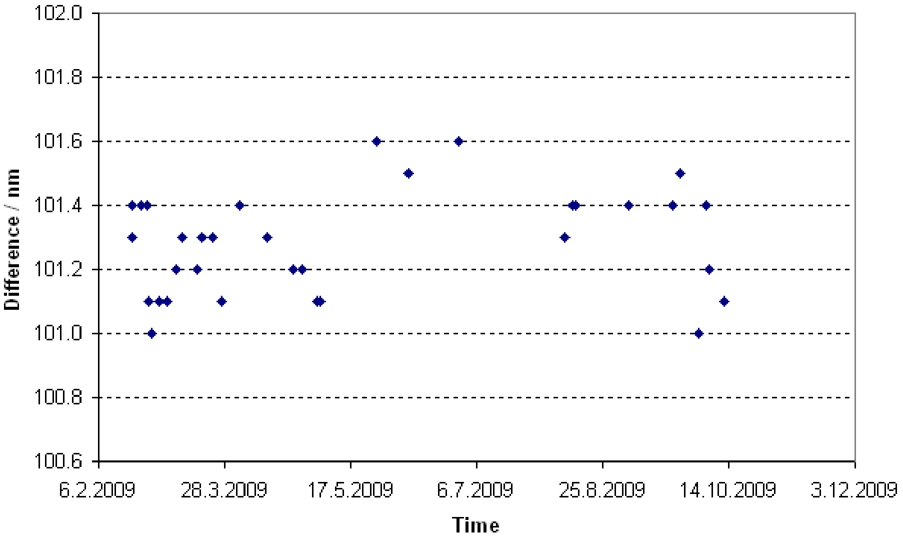

Figure 8.7. The difference between the measured air gap values has been stable during the eight-month test period. The largest variation was 0.3 nm from the average difference of 101.3 nm.

The control voltages for the piezoelectric actuators were also measured during the test together with the humidity. Measured control voltages are shown in Figure 8.8 as a function of the humidity for the measurement between March and July. The voltage needed for the same air gap varies according to the humidity of the environment.

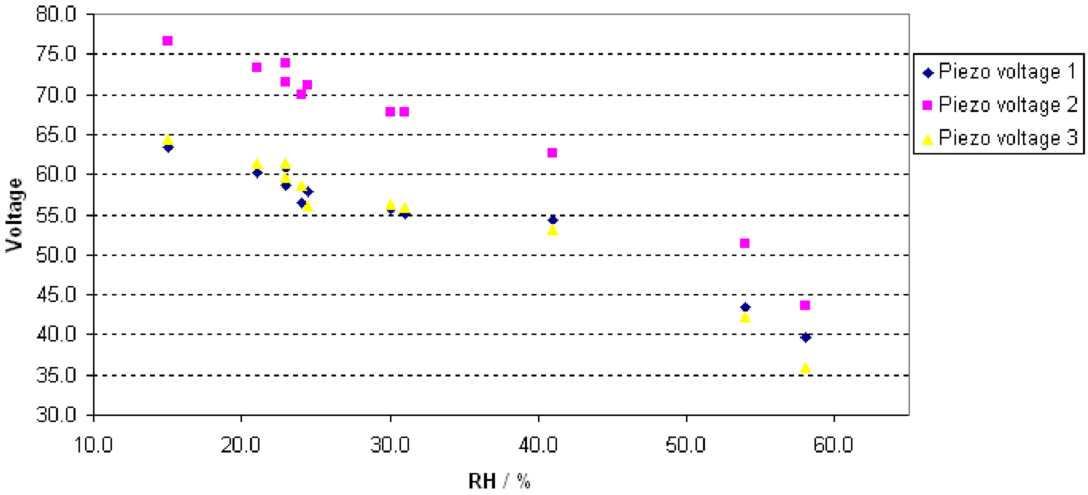

Figure 8.8. During the endurance test the control voltages for the piezoelectric actuators were noticed to vary according to the humidity of the environment.

8.4 Settling Time of the Interferometer Module

Settling time of the Fabry-Perot interferometer was measured for a 200 nm step change. The air gap is changed by applying a step in the gap set point. This creates an error signal in the output of each capacitive half bridge. The error signal amplitude is relative to the error in the air gap and can be used to estimate the settling time of the interferometer module. The settling time was measured with an oscilloscope from the output of the buffer amplifier of the gap controller board. The error signal is shown in Figure 8.9. Due to the low pass filter shown in Figure 6.5 the change in the error signal is not instantaneous when the set point values are changed. The settling time was approximated to 0.6 ms from the measured signal.

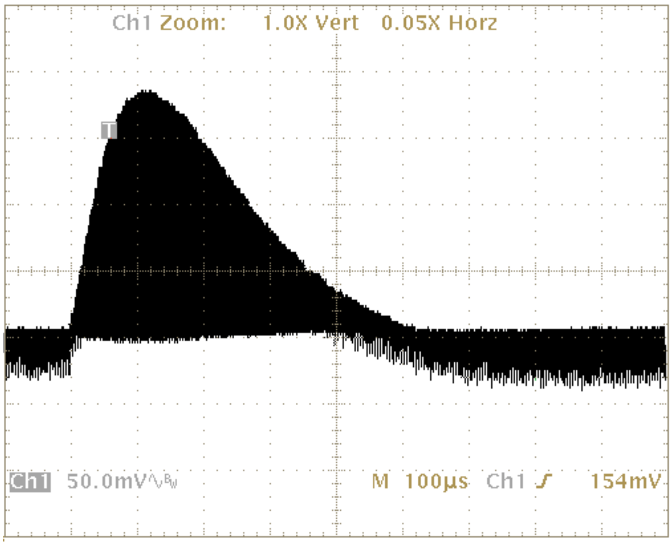

Figure 8.9. The error signal measured at the output of the buffer amplifier. The amplitude of the error signal is relative to the error in the air gap. The settling time for a step change was approximated to 0.6 ms.

8.5 Average Power Consumption

The average power consumption of the instrument was measured in the imaging mode with continuous saving of image data. This is the mode with the highest power consumption. The average power consumption is approximately 1.6 W using a 7.2 V lithium-ion battery as the power supply. This is well below the 3 W requirement set for the imager.

8.6 Summary

Table 8.1 summarises the requirements set for the hyperspectral imager together with the measured values. Most of the requirements were fulfilled but the reproducibility of the air gap was not as good as required. This is mostly caused by the open structure of the interferometer module and the temperature drift of the reference capacitors. Therefore one of the future tasks will be to mount the interferometer module in a hermetically sealed enclosure. Different temperature stabilization and compensation methods should also be considered in order to minimize temperature and humidity induced drift. The noise induced mirror movement was estimated for the noise measured from the preamplifier output. This RMS movement was estimated to 0.1 nm. The RMS noise of the air gap measurement system is approximately 0.05 nm.

Table 8.1. Requirements and the measured values for the hyperspectral imager.

Parameter	**Requirement**	**Measured value**
Spectral sampling step size	< 1 nm	0.2 nm
Reproducibility of the air gap	< 0.5 nm	2 nm
Time required to change the wavelength band	< 2 ms	0.6 ms
Average power consumption	< 3 W	1.6 W
Maximum envelope without objective	< 110 mm x 75 mm x 55 mm	110 mm x 75 mm x 55 mm
Mass of the instrument	< 350 g	302 g

9 The Hyperspectral Imager Tests

At the end of September 2009 the hyperspectral imager was taken to Belgium for a common test campaign of VTT and VITO (Flemish Institute for Technological Research, Mol, Belgium, www.vito.be). The imager was mounted on a Draganfly X6 UAV helicopter to test the system applicability for hyperspectral data acquisition from a UAV [33]. Figure 9.1 shows the imager mounted below the helicopter. One of the objectives was to evaluate the geometric and radiometric properties of the imager with reference targets. For UAV applications additional data processing is needed as the aircraft moves during the data acquisition. Therefore the sequentially gathered images contain spectral data from slightly different areas. To acquire the spectrum for a certain pixel different images need to be aligned before the spectral data is valid. This data processing will be done in the near future for the data gathered from the flights.

Figure 9.1. The hyperspectral imager was mounted on a UAV helicopter for test flights. The mass of the hyperspectral imager including the battery is 350g so it can be easily carried by the helicopter.

Other tests were made by mounting the imager on top of a telescope mast which could be extracted to a length of 10 m. This setup was used to obtain hyperspectral data from various test sites. Figure 9.2 shows the test setup and part of the hyperspectral data acquired over a pear tree. Leafs of the pear tree reflect strongly in the near infrared region of the spectrum which can be seen in Figure 9.2 d). This is a common spectral feature for vegetation. The spectral signal has dips near the wavelengths 760 nm and 820 nm which are caused by the oxygen and water vapour absorption in the atmosphere respectively. Natural objects have different spectral signatures and, therefore, the hyperspectral imager can be used for target identification as well as for spatial discrimination of different objects in the observed area. The spectrum acquired from the surface of the pavement is shown in Figure 9.2 c).

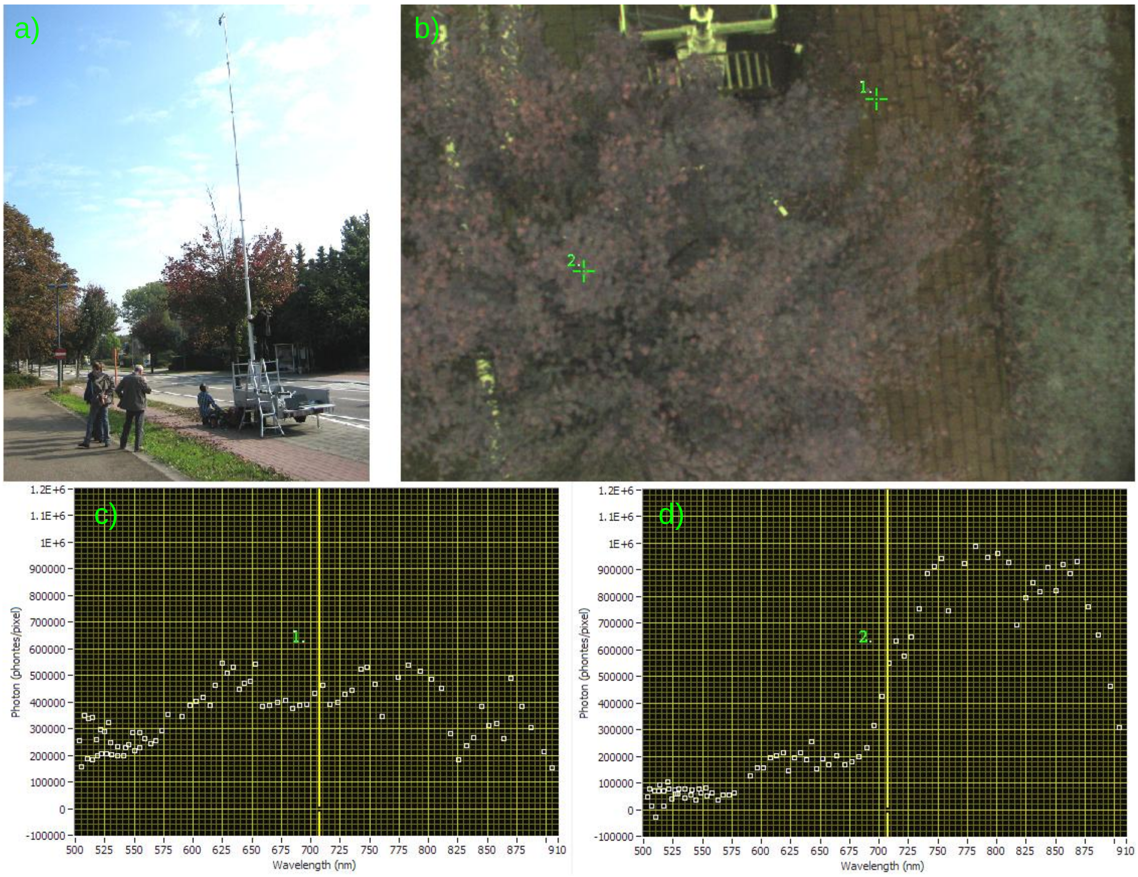

Figure 9.2. a) The hyperspectral imager was mounted on top of a telescope mast to gather hyperspectral data from a pear tree. b) The false-colour image was taken with the hyperspectral imager aiming straight down from the mast. The spectrum in diagram c) is from the surface of the pavement and diagram d) shows the spectrum of leafs.

Figure 9.3 shows the spectra of a red shirt and a blue coat. The red shirt has high signal at the range of 620 nm – 750 nm which is the wavelength region for the red colour. The blue region (400 nm – 500 nm) of the spectrum is filtered out of the image as the hyperspectral imager was configured for the wavelength range from 500 nm to 910 nm.

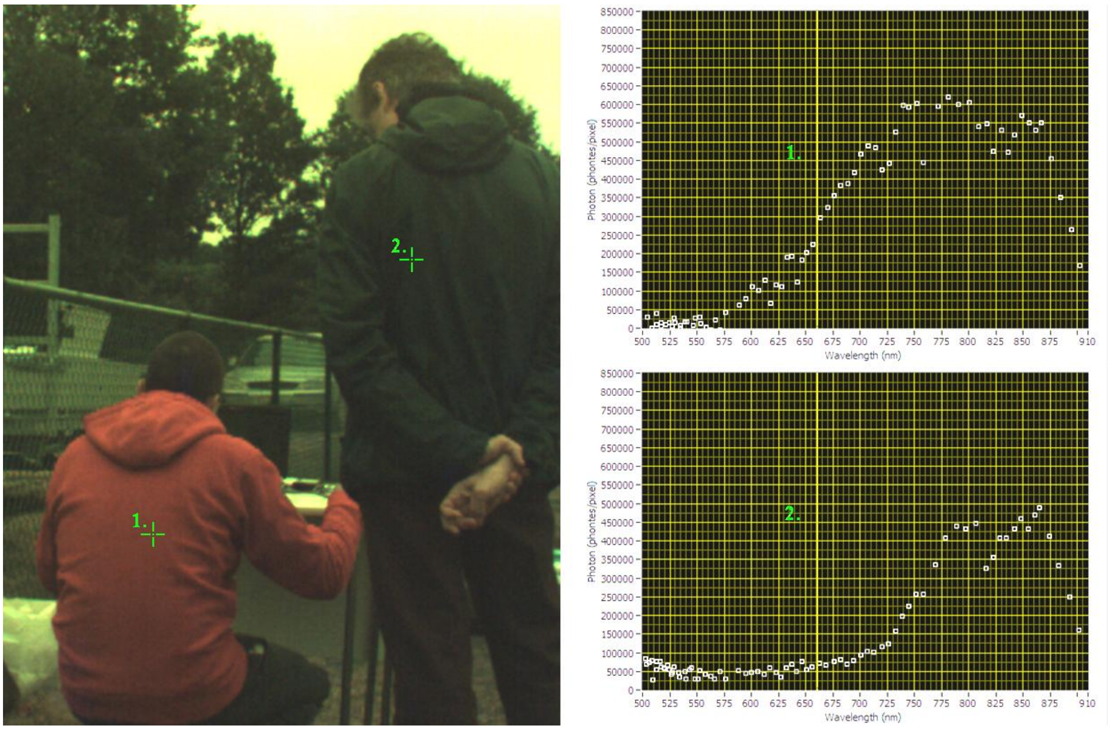

Figure 9.3. The raw image shown on the left side is taken with the hyperspectral imager with one of the interferometer air gaps. On the right side are the spectra acquired from the red shirt and the blue coat.

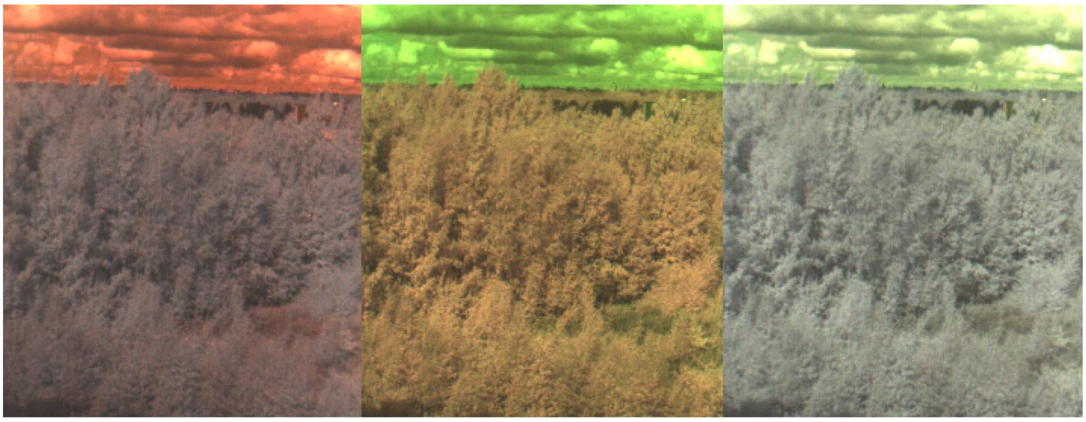

Figure 9.4. Raw images acquired from a scenery with the hyperspectral imager. Each image contains spectral data from three different wavelength bands.

Figure 9.4 shows three raw images acquired from a forest with the hyperspectral imager. These false-colour images can be used to estimate the spectral content of the scenery at nine spectral wavelength bands.

10 Conclusions

In this work the control electronics were designed for a hyperspectral imager. The concept utilizes the combination of a Fabry-Perot interferometer and an RGB-image sensor to capture the spectral data. A three-channel closed-loop control system was designed for the interferometer module to control the transmitted wavelengths. A previously developed imaging platform was modified to include a flash memory to store image data. The hyperspectral data cube can be calculated from the acquired raw data during post processing.

Important performance parameters for the hyperspectral imager control electronics were measured. With 16-bit digital-to-analogue converters it is possible to control the air gap of the Fabry-Perot interferometer with a step size of approximately 0.2 nm. For the second order transmission peak this corresponds to a step size of 0.2 nm in the central wavelength. For higher order transmission peaks the sampling step size is smaller. The reproducibility of the air gap was also measured in three different tests. Temperature drift for one of the interferometer modules was measured to be approximately 0.5 nm/°C in one position of the interferometer aperture which is mainly caused by the temperature characteristics of the reference capacitors. The temperature drift is different for each control channel as the characteristics of the reference capacitors are not identical. Therefore, the mirror parallelism also changes with the temperature. In a short time period the RMS variation of the air gap has been observed to be 0.1 nm around the set point. The interferometer drift was also tested in an eight-month endurance test. After a one week burn-in period the air gap varied by less than 1 nm from the average position during a four month period. After this period the measured air gap values showed an increase in the variation. This might be an indication of the multilayer piezoelectric actuator losing its integrity. During the tests it was noticed that the control voltages of the piezoelectric actuators vary according to the humidity of the environment. This changes the usable air gap range of the interferometer.

The settling time for a 200 nm step change in the interferometer air gap was measured to be 0.6 ms. This determines the wait time before a new exposure after a change in the air gap. The achieved frame rate for the imager was 20 fps. In the continuous imaging mode the power consumption of the hyperspectral imager was 1.6 W. The system weight was 302 g excluding the battery. This is one of the most compact hyperspectral imagers of this kind.

The stability for the interferometer requires further improvements as it was noticed that the air gap changes with the temperature. The effects of the humidity should also be minimized. Therefore, the interferometer module should be enclosed in a hermetically sealed package filled with a protective gas. Temperature effects could be compensated with software if the temperature characteristics are known for each channel. The set point values used for different control channels can be adjusted as a function of the measured temperature to compensate for temperature changes. With individual compensation for each channel the mirror parallelism could be maintained. Temperature stabilization could also be used to keep the interferometer module and the reference capacitors in a known temperature. However, this would increase the power consumption of the system.

Currently, the flash memory limits the maximum achievable frame rate. Especially in UAV-imaging applications higher frame rate would provide a larger overlap between different wavelength layers in the raw data cube. Individual data cubes could then be more easily processed. The data rate could be improved, for example, by using a fast cache memory to save images for one data cube. After the short data acquisition phase the data could be transferred to a flash memory. A low noise image sensor with higher sensitivity could be used to decrease the integration time of the sensor.

The small size and low cost of the system opens up new interesting fields of application for hyperspectral imaging. The imager can, for example, be connected to a microscope to gather spectral data from biologic samples. In a similar way the platform can be used as part of diagnostic test readers where the imager is configured to detect certain interesting properties of the target spectrum. The lightweight UAV-imaging system opens up new possibilities for environment monitoring.

Bibliography

[1] M. R. Descour and E. L. Dereniak, *Nonscanning no-moving-parts imaging spectrometer*, Imaging Spectrometry, Proc.SPIE Vol. 2480, p. 48-64, 1995.

[2] J. Nieke, H. Schwarzer, A. Neumann and G. Zimmermann, *Imaging Spaceborne and Airborne Sensor Systems in the Beginning of the Next Century*, Proc. SPIE Vol. 3221, p. 581-592, 1997. Sensors, Systems, and Next-Generation Satellites.

[3] E. Hecht, *Optics*, fourth edition, Addison Wesley, 2002.

[4] Frank L.Pedrotti, Leno S. Pedrotti, Leno M. Pedrotti, *Introduction to Optics*, third edition, Pearson Prentice Hall, 2007.

[5] P. Jacquinot, *New developments in interference spectroscopy*, Rep. Prog. Phys. 23, p. 267-312, 1960.

[6] S. O. Kasap, *Optoelectronics and Photonics: Principles and Practices*, Prentice Hall, 2001.

[7] Keigo Iizuka, *Elements of photonics*, *Vol.1*, *In free space and special media*, Wiley series in pure and applied optics, 2002.

[8] E. Ikonen, *Optiikan perusteet,* Helsinki University of Technology, 2006.

[9] J. J. Monzón, L. L. Sánchez-Soto and E. Bernabeu, *Influence of coating thickness on the performance of a Fabry–Perot interferometer*, Appl. Opt. 30, p. 4126-4132, 1991.

[10] H. Saari *et al.*, *Novel miniaturized hyperspectral sensor for UAV and space applications*, Proc. SPIE 7474, To be published 2009.

[11] H. Saari, *Spectrometer and interferometric method*, Patent FI119830B, 2009.

[12] X. Prieto-Blanco, C. Montero-Orille, B. Couce and R. de la Fuente, *Optical configurations for Imaging Spectrometers*, Comput. Intel. For Remote Sensing SCI, vol. 133, p. 1-25, Springer-Verlag, Heidelberg 2008.

[13] Mars Science Laboratory Instruments: MastCam, September 2009. [Online]. Available: http://martianchronicles.wordpress.com/2009/09/16/mars-science-laboratory-instruments-mastcam/

[14] Micron, *MT9V022 image sensor*, datasheet: January 2006. [Online]. Available: http://www.1stvision.com/cameras/sensor_specs/Micron_MT9V022.pdf

[15] J. E. Mack, D. P. McNutt, F. L. Roesler and R. Chabbal, *The PEPSIOS Purely Interferometric High-Resolution Scanning Spectrometer. 1. The Pilot Model*, Applied Optics, Vol. 2, p. 873-885, 1963.

[16] Noliac group, *Piezo materials-Basic of materials*, October 2009 [Online] Available: http://www.noliac.com/Basics_of_materials-6585.aspx

[17] J. G. Winter, *Servocontrol of a Fabry-Perot interferometer*, J. Phys. E: Sci. Instrum. 18, p. 505-509, 1985.

[18] T. R. Hicks, N. K. Reay and R. J. Scaddan, *A servo controlled Fabry-Perot interferometer using capacitance micrometers for error detection*, J. Phys. E: Sci. Instrum. 7, p. 27-30, 1974.

[19] D. Rees, I. McWhirter, P. B. Hays and T. Dines, *A stable, rugged, capacitance-stabilised piezoelectric scanned Fabry-Perot etalon*, J. Phys. E: Sci. Instrum. 14**,** p. 1320-1325, 1981.

[20] C. Holmlund, personal discussion, VTT optical instruments, Espoo, 2008.

[21] NXP Semiconductors, *BF545 N-channel J-FET,* Datasheet, Rev. 03, August 2004. [Online]. Available: http://www.nxp.com/acrobat_download/datasheets /BF545A_BF545B_BF545C_3.pdf

[22] Analog Devices, *ADR361 Voltage Reference*, Datasheet, Rev. C, July 2007. [Online]. Available: http://www.analog.com/static/imported-files/data_sheets/ ADR360_361_363_364_365_366.pdf

[23] Analog Devices, *AD5662 Digital to Analog Converter,* Datasheet, Rev. 0, January 2005. [Online]. Available: http://www.analog.com/static/imported-files/ data_sheets/AD5662.pdf

[24] Atmel Corporation, *ATtiny24,* Datasheet, Rev. 8006H, October 2009. [Online]. Available: http://www.atmel.com/dyn/resources/prod_documents/doc8006.pdf

[25] Maxim Integrated Products, *MAX668 DC-DC Converter,* Datasheet, Rev 1, January 2002. [Online]. Available: http://datasheets.maxim-ic.com/en/ds/ MAX668-MAX669.pdf

[26] International Rectifier, *IRF7811 Power MOSFET,* Datasheet, June 2009. [Online]. Available: http://www.irf.com/product-info/datasheets/data/irf7811w.pdf

[27] *Soft Ferrites*, Components Data Handbook, 1993.

[28] ONFI, *Open NAND Flash Interface Specification*, [Online]. December 2006, Available: http://onfi.org/wp-content/uploads/2009/02/onfi_1_0_gold.pdf

[29] Micron Technology Inc., *NAND Flash Memory*, Datasheet, Rev B, February 2007. [Online]. Available: http://download.micron.com/pdf/datasheets/flash/nand/4gb_nand_m40a.pdf

[30] NXP Semiconductor, *LPC2129 32-bit ARM 7 microcontroller*, Datasheet, Rev 6, December 2007. [Online]. Available: http://www.nxp.com/acrobat_download/datasheets/LPC2109_2119_2129_6.pdf

[31] Xilinx Inc., *XCR3256XL 256 Macrocell CPLD*, Datasheet, v2.7, March 2006. [Online]. Available: http://www.xilinx.com/support/documentation/data_sheets/ds013.pdf

[32] Bitwise Systems, *QuickUSB User Guide*, version 2.11.41, April 2007. [Online]. Available: http://www.quickusb.com/media/QuickUSB_User_Guide_v2.11.41.pdf

[33] H. Saari et al., *New Hyperspectral Imager for Light Weight UAVs – First test flight results*, Proc. Nordic Remote Sensing Days, 22.-23. October 2009, Helsinki, Available: http://www.kaukokartoituskerho.fi/sites/default/files/Saari.pdf.

Appendix A

Hyperspectral Imager Parts

The assembled PCBs and other parts of the hyperspectral imager are presented in this section. The preamplifier board and the Fabry-Perot interferometer module are shown in Figure A.1 together with the image sensor.

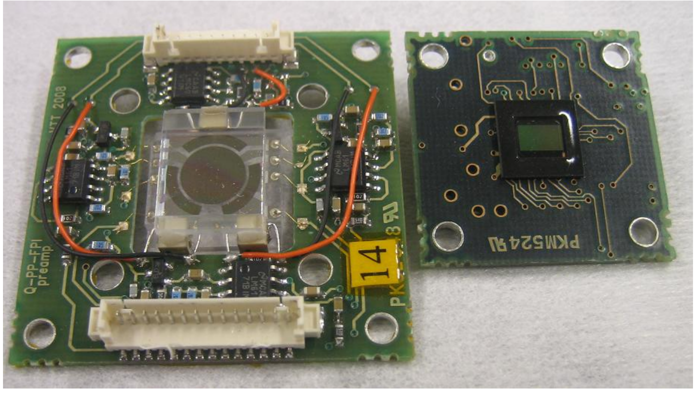

Figure A.1. The preamplifier board and the interferometer module are on the left and the image sensor is on the right.

The gap controller board and the flash memory card are shown in Figures A.2 and A.3.

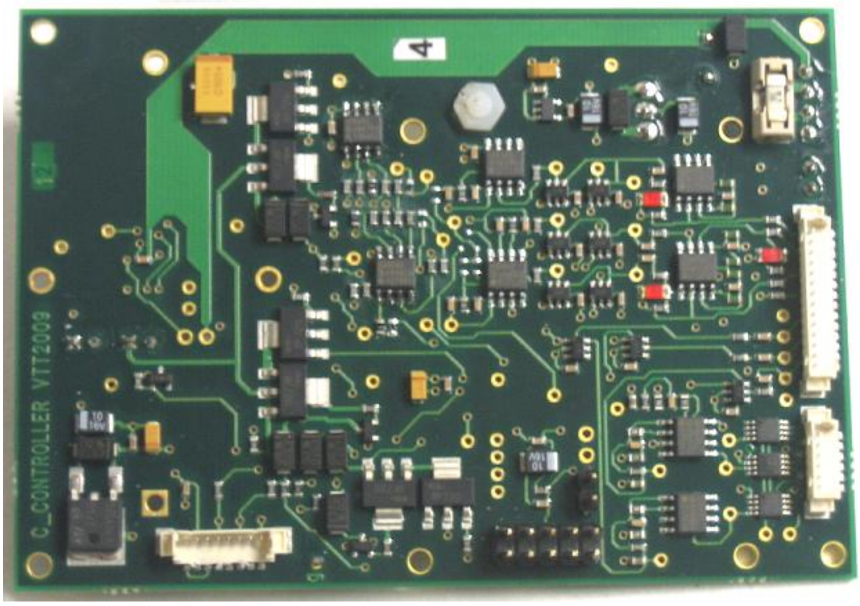

Figure A.2. The gap controller board.

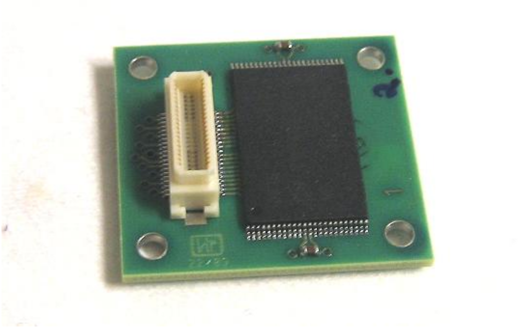

Figure A.3. The flash memory card.

The spectrometer control board electronics and layout were modified by the author to accommodate the flash memory card. The memory card is used as data storage for the imager. Spectrometer control board is shown in Figure A.4.

Figure A.4. The spectrometer control board.

The hyperspectral imager frame and the objective for the imager are shown in Figure A.5. The assembled imager is shown in Figure A.6.

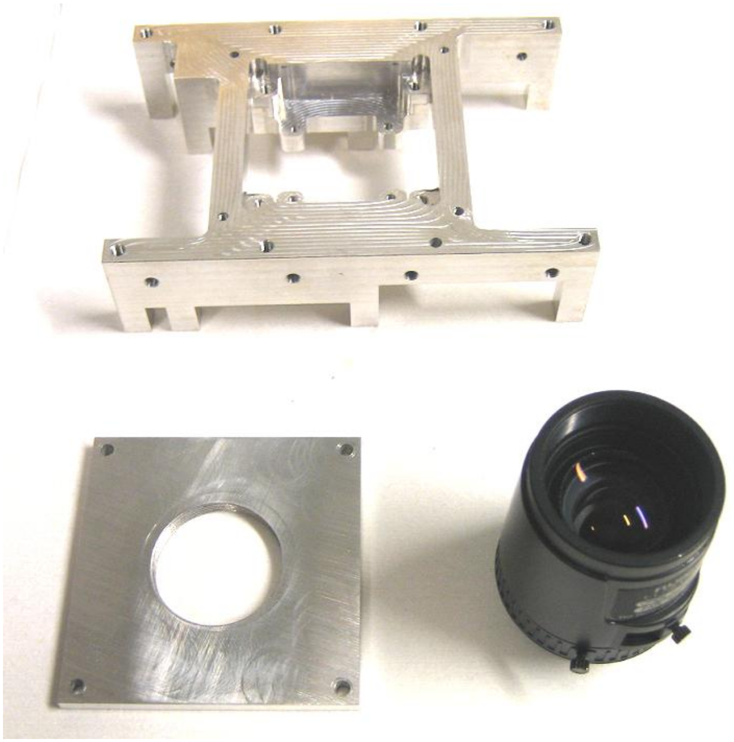

Figure A.5. The hyperspectral imager frame and the objective.

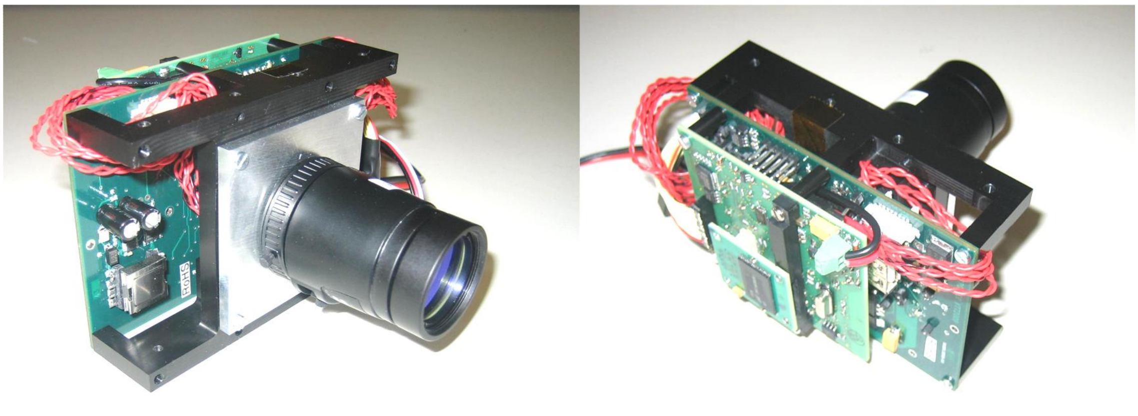

Figure A.6. The assembled hyperspectral imager.

Appendix B

Preamplifier Noise and the Equivalent Change in the Air Gap

The gap controller considers the noise in the error signal as an error in the interferometer air gap. This causes a random movement in the mirrors. The frequency response of the control loop limits the effect of the high frequency noise. Figure B.1 shows the control loop and the noise V_{no} at the preamplifier output. The RMS noise at the preamplifier output was 217 µV in the frequency range from 10 kHz to 10 MHz measured with a Hewlett Packard 89410A Vector signal analyzer. This chapter shows how to approximate the equivalent mirror movement.

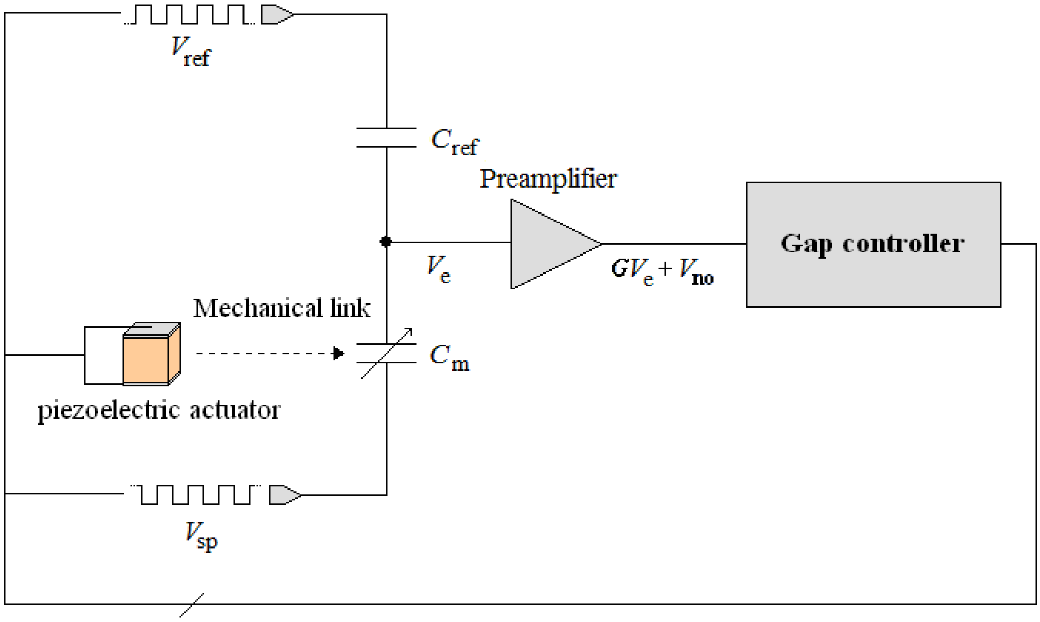

Figure B.1. The signal at the preamplifier output contains the amplified error signal and noise. The noise is interpreted also as an error in the air gap and the control loop moves the mirrors due to this noise.

The mirror movement Δd caused by the noise is estimated as a movement which causes an error voltage with equivalent amplitude at the preamplifier output. This corresponds to the correction made by the control loop to minimize the error voltage. The mirror movement is calculated for the equilibrium condition where $C_m = C_{ref} = 8$ pF. According to Equation 5.5 the set point voltage V_{sp} equals the reference voltage, V_{ref}, when $C_m = C_{ref}$. In the balance conditions the error signal amplitude V_e is zero. When the mirror moves a distance Δd the capacitance changes by ΔC. According to Equation 5.4 this will cause an error signal V_e which can be written as

$$V_\mathrm{e} = \frac{C_\mathrm{ref} V_\mathrm{ref} + \left(C_\mathrm{m} + \Delta C\right) V_\mathrm{sp}}{C_\mathrm{m} + C_\mathrm{ref}} . \tag{B.1}$$

With the substitution $C_\mathrm{m} = C_\mathrm{ref}$ and $V_\mathrm{ref} = -V_\mathrm{sp}$ the equation reduces to

$$V_\mathrm{e} = \frac{\Delta C V_\mathrm{sp}}{2 C_\mathrm{ref} + \Delta C} . \tag{B.2}$$

The capacitance C_m can be approximated with Equation 5.3 as

$$C_\mathrm{m} \approx \varepsilon_0 \frac{A_\mathrm{r}}{2d} , \tag{B.3}$$

where d is the air gap. With this approximation the change in the capacitance can be solved as

$$\Delta C = \frac{\varepsilon_0 A_\mathrm{r}}{2} \left(\frac{1}{d + \Delta d} - \frac{1}{d} \right), \tag{B.4}$$

For two electrodes the common area is A_r which is approximated from the coating mask files which are used to manufacture the mirrors. Figure B.2 shows the two mirrors and surrounding electrodes aligned on top of each other. The common area A_r for the electrodes was 3.5mm^2.

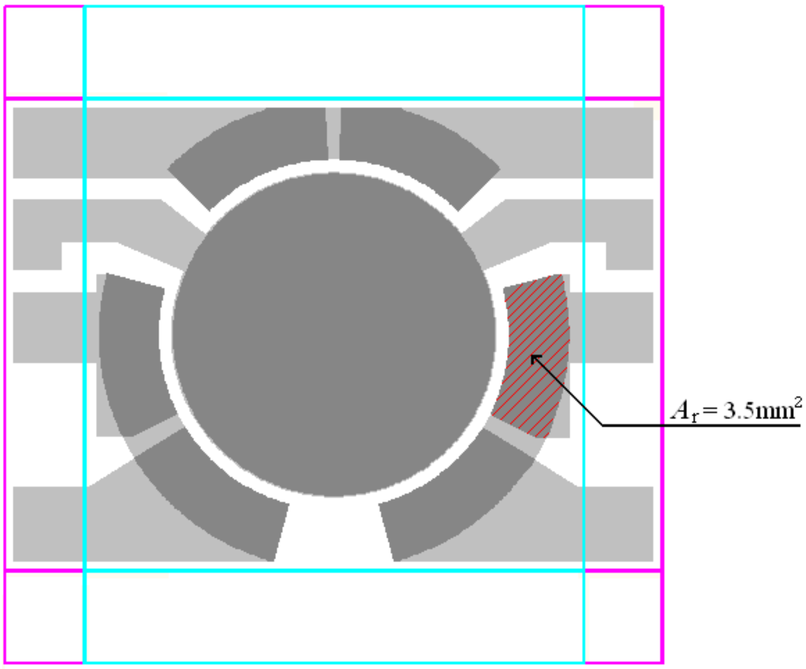

Figure B.2. The Q-PP-FPI module mirrors aligned on top of each other. The estimated common area of two electrodes is shown in the picture.

The air gap for this capacitor area in balance conditions can be solved from Equation 5.6 as

$$d = \frac{A_r \varepsilon_0}{2C_{\text{ref}}}. \tag{B.5}$$

From Equations B.2, B.4 and B.5 the air gap fluctuation Δd can be written as

$$\Delta d = \frac{\varepsilon_0 A_r V_e}{C_{\text{ref}}\left(V_{\text{sp}} - 3V_e\right)}. \tag{B.6}$$

In the equilibrium conditions V_{sp} = -V_{ref} = 2.5V and the permittivity of vacuum ε_0 is 8.8541×10^{-12} F/m. The error voltage V_e that causes a voltage of 217 µV at the preamplifier output is 217 µV / 3.2 = 67.8 µV, where the denumerator is the gain of the preamplifier. With these values the RMS mirror movement Δd was approximated to be 0.1 nm.